CHALMERS
UNIVERSITY OF TECHNOLOGY

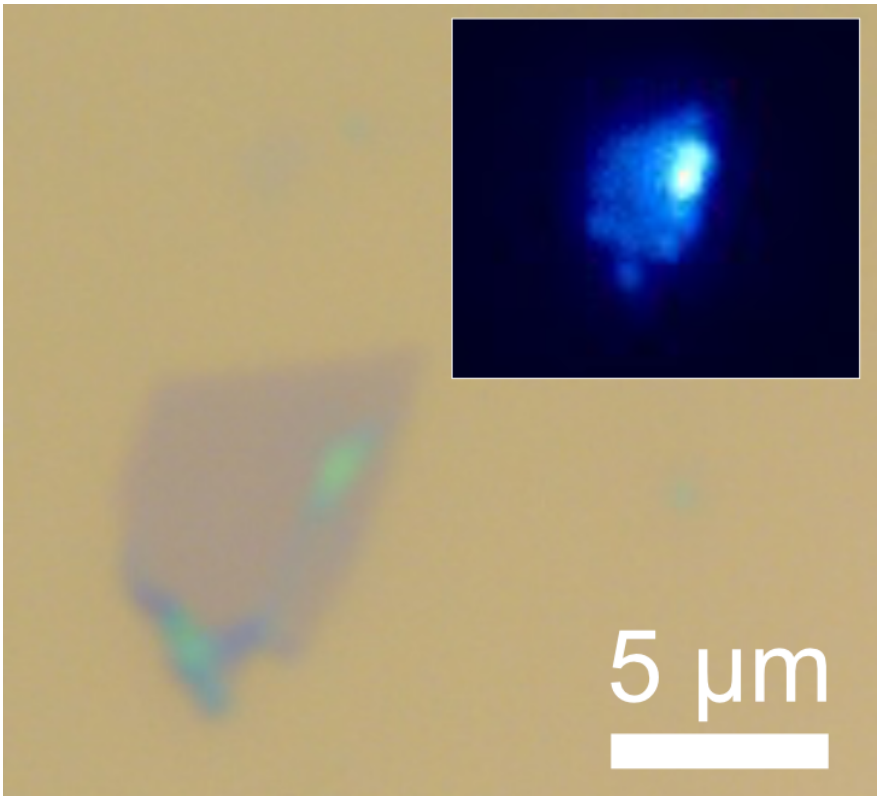

Optical characterisation of two-dimensional WSe_2 flakes for quantum light emission

Master's thesis in Chalmers Nanotechnology Master's Programme

JOEY FREY

Department of Microtechnology and Nanoscience
CHALMERS UNIVERSITY OF TECHNOLOGY
Gothenburg, Sweden 2020

Master's thesis 2020

Optical characterisation of two-dimensional WSe_2 flakes for quantum light emission

JOEY FREY

CHALMERS
UNIVERSITY OF TECHNOLOGY

Department of Microtechnology and Nanoscience
Division of Quantum Technology Laboratory
Witlef Wieczorek's lab group
Chalmers University of Technology
Gothenburg, Sweden 2020

Optical characterisation of two-dimensional WSe_2 flakes for quantum light emission
JOEY FREY

Supervisor & examiner: Witlef Wieczorek, MC2 Department, Chalmers
Assistant supervisor: Hanlin Fang, MC2 Department, Chalmers

Master's Thesis 2020
Department of Microtechnology and Nanoscience
Division of Quantum Technology Laboratory
Witlef Wieczorek's lab group
Chalmers University of Technology
SE-412 96 Gothenburg
Telephone +46 31 772 1000

Cover: *Image of a monolayer WSe_2 flake placed onto a nanopillar. Inset: Photoluminescence map of the sample.*

Typeset in LaTeX
Printed by Chalmers Reproservice
Gothenburg, Sweden 2020

Optical characterization of two-dimensional WSe_2 flakes for quantum light emission
JOEY FREY
Department of Microtechnology and Nanoscience (MC2)
Chalmers University of Technology

Abstract

Two-dimensional (2D) materials are atomically thin materials that have received a lot of attention over the last decade due to their unique properties. Especially interesting for optics are semiconducting transition metal dichalcogenides, which show strong photoluminescence in monolayer form due to their direct band gap. Further, weak screening effects in 2D materials lead to strongly bound electron-hole pairs, called excitons. Recently, photoluminescence studies in WSe_2 flakes noticed that localised emitters could be found at the edges of such flakes. The emitters were investigated with a Hanbury Brown & Twiss set-up which showed that they were single photon emitters: non-classical light sources only able to emit one photon at a time by radiative recombination of a localised exciton.
Single photon emitters are very sought after in quantum technologies and can be used for flying qubits in quantum computing or for quantum cryptography. 2D materials show promise as novel materials enabling single photon emission because they are optically active on the surface and can be used with current on-chip technology compared to single photon emitters in quantum dots or diamond nitrogen vacancy centres.
The goal of this work is to characterise photoluminescence emission in WSe_2 flakes and to explore first steps towards engineering 2D-based quantum emitters in this material system. To this end, a micro-photoluminescence set-up is built and optimised to characterise non-resonant light emission from 2D materials and its time correlations. Large area excitation is used to generate a photoluminescence map which reveals localised emitters in strained mono- and fewlayer WSe_2 flakes. Moreover, by taking temperature-dependent photoluminescence spectra we see defect emission emerging at low temperatures (< 30 K). The emission centers show sharp emission peaks and saturation behavior, which is indicative of single photon emission. From time-dependent photoluminescence measurements lifetimes of between 0.48-10.6 ns are identified, which is consistent with those of localised excitons reported in other studies. The emitters show low spectral wandering, but change their position after cycling from 4 K to room temperature and back.
This work examined the initial characterisation of non-classical light emission in WSe_2 flakes. Future steps in the investigation of 2D quantum emitters could be focused on moiré based emitters or integration into photonic chips.

Keywords: 2D material, Micro-Photoluminescence, Quantum Optics, Single Photon Emission, Transition metal dichalcogenide, WSe_2.

Acknowledgements

First, I would like to thank my supervisor and examiner Assistant Prof. Witlef Wieczorek, who has been a great support and gave me the opportunity to research an incredibly fascinating field. Thanks to your insight and feedback I have been provided with the possibility to improve and grow, for which I am very grateful. Secondly, I would like to thank my co-supervisor Postdoc. Hanlin Fang who has helped and guided me daily during the course of my thesis. He has been a great mentor to me and has always offered his time for discussions and feedback.
Next, I would like to thank Marti who has always been helpful and instructive for my work in the laboratory and especially with the cryostat. I also thank you for the many interesting discussions that we had. I am also grateful to Sushanth who has assisted me in the laboratory and given me helpful advice.
I would then like to thank everyone who worked with us in researching quantum light emission in 2D materials: Associate Prof. Saroj Prasad Dash for the important input into the fabrication of the samples as well as Prof. Ermin Malic and Research Associate Joshua Thompson for providing the theoretical insight into our work.
Additionally, I would like to thank Chalmers for providing me with five great years. During my time here, I have been provided a great opportunity to learn interesting subjects, meet amazing people and grow in many different roles.
Then, I want to express my gratitude to all my amazing friends who have motivated and been there for me during my time at Chalmers. Without my friends to talk and laugh with, it would not have been possible for me to make it through these five years.
Lastly, I would like to thank my family who has always supported and encouraged me in all my aspiration. With you there, I have never needed to hesitate in the face of new challenges.

Joey Frey, Gothenburg, 06/2020

Contents

List of Figures

List of Tables

List of abbreviations

2D	Two-dimensional
AFM	Atomic Force Microscopy
APO	Apochromat
BS	Beamsplitter
BZ	Brillouin Zone
CB	Conduction Band
CBM	Conduction Band Minimum
CCD	Charge-Coupled Device
CVD	Chemical Vapor Deposition
CW	Continuous Wave
EBL	Electron Beam Lithography
FL	Fewlayer
FWHM	Full Width at Half Maximum
hBN	Hexagonal Boron Nitride
IRF	Intstrument Response Function
LED	Light-Emitting Diode
LT	Low Temperature
OD	Optical Density
PIC	Photonic Integrated Circuit
PL	Photoluminescence
QD	Quantum Dot
QE	Quantum Efficiency
QKD	Quantum Key Distribution
RT	Room Temperature
SEM	Scanning Electron Microscope
SPAPD	Single Photon Avalanche Photodiode
SPE	Single Photon Emitter
TDC	Time-to-Digital Converter
TMD	Transition Metal Dichalcogenide
TRPL	Time Resolved Photoluminescence
VB	Valence Band
VBM	Valence Band Maximum

1

Introduction

For centuries, people have investigated the properties of light and used their knowledge to model and engineer the interaction between light and matter. Subsequently, technological advancements have allowed humans to advance into an age where instantaneous world-wide communication and pocket-sized high resolution displays are part of every-day life. However, as technology has improved, so has the demand for performance & security of optical-, photonic- and optoelectronic devices.

Since the invention of the computer, communication and massive data handling has become more and more efficient. But everything has a limit, and classical computers are starting to reach theirs with current transistors approaching nanometer sizes [1]. These limitations of classical computers were predicted and as early as the 80s famous scientists such as Feynmann [2] suggested computation with quantum bits, *qubits*, as an alternative. Using superposition, some computations could be finished exponentially faster than classical computers. At the end of the 90s, applications of quantum computing such as Shor's algorithm [3] was starting to come forward and the interest for quantum technologies grew quickly. Additionally, secure communications can be achieved by exchanging utilising quantum cryptography, where the "key" to decrypt information is sent with quantum transmission. The information is then safe as it can not be monitored without disturbing the state of the system [4].

Light is appealing for use in quantum information and quantum encryption technologies. Information can be coded into the various degrees of freedom of light such as *polarisation*, *orbital angular momentum*, *photon number* and *time* [5]. Light is easily manipulated and does not interact with the environment which presents an advantage to many other quantum systems due to long decoherence times. Additionally, light allows for long-distance quantum communication as "flying qubits" and transfers information with, well, the speed of light.

When discussing light in quantum technologies, an important concept is that of single photons. Statistically, the definition of the single photon state is where the mean number of photons is one, with a variance of zero [6]. This is called a Fock state or photon number state of one photon. Single photon sources exhibit "antibunching", a phenomenon where two photons have a lowered probability of being emitted within a short timespan. Photon statistics can be studied with the second-order coherence function, $g^{(2)}(\tau)$, which correlates the intensity of light at two points in time and space. A Hanbury Brown & Twiss set-up is used for this purpose, where light is split in two paths by a 50:50 beamsplitter with a single photon detector in each path. Sources with single photon emission will then generate anticorrelation at zero time

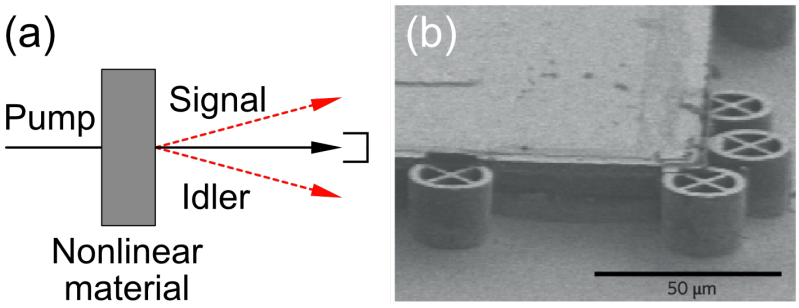

Figure 1.1: a) Illustration of the working principle of parametric down-conversion. One photon is converted to two output photons, while energy is conserved. If one of the photons is detected, the other can be used as a single photon. **b)** SEM image of four pillar cavities with quantum dots inside them. Taken from ref. [12].

delay, resulting in $g^{(2)}(\tau = 0) = 0$.

Single photons emitters (SPE) are required for applications of quantum cryptography protocols such as the BB84 for quantum key distribution (QKD) [7] or for implementations of optical quantum computing such as the Knill-Laflamme-Milburn (KLM) scheme [8]. Thus, since the 1990s when research in quantum computing and quantum cryptography took off, so did research into single photon sources [6].

An important distinction is often made between probabilistic and deterministic single photon sources. Probabilistic sources generate single photon pairs with some finite probability, by methods such as four-wave mixing (FWM) or parametric down-conversion (PDC) [5]. These sources work by converting one or two pump photons to two photons and respecting energy conservation, illustrated for PDC in figure 1.1a). However, these sources will have a nonzero probability of generating more than one photon, which increases with the probability of generating single photons [6]. Therefore, generally low single photon yield is used to avoid multi-photon generation.

Deterministic photon sources will in the ideal case, generate emission "on demand", with zero probability of multiple-photon emission. Additionally the photons should be indistinguishable, with fast repetition rate [6]. The most common deterministic single photon sources today are trapped ions [9], color centers [10] and quantum dots (QDs) [11, 12]. In figure 1.1b) quantum dots embedded into pillar cavities are shown, which can be electrically controlled to generate single photon emission [13] and are commercially available products.

Currently, the most reliable method to generate single photons are with QD sources, which have high single photon purity [14] and near-unity indistinguishably [15] but must be operated at cryogenic temperatures (< 10 K). The single photons are collected off-chip however, and considerable effort is directed towards the integration of QDs on a single photonic chip [16]. Photonic circuits are appealing as normally large scale optical elements such as beamsplitters and mirrors can be integrated on-chip, yielding a compact optical system [17]. However, integration onto photonic chips has been proven difficult for solid state emitters such as QDs and color centers. Current solutions include cost-inefficient individual emitter placement in photonic

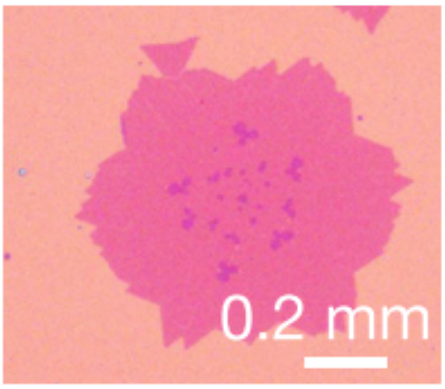

Figure 1.2: Monolayer flake of TMD material WSe_2 grown epitaxially with chemical vapor deposition. Taken from ref [27].

integrated circuits (PICs), which suffer from low scalability [18].

A novel source for single photon emission was recently discovered in the field of two-dimensional (2D) materials, first in transition metal dichalcogenides (TMDs) in 2015 [19–23] and then in hexagonal boron nitride (hBN) in 2016 [24]. These materials have atomic thickness and get their name from that fact. Their large surface area makes them susceptible to influence from their environment, which can be utilized for engineering the properties of these materials [25]. Due to the absence of dangling bonds on the surface, 2D materials are mostly nonreactive and bind together weakly with van der Waals interaction to form bulk crystals. Monolayer flakes can therefore be produced in a simple and cheap way by repeated peeling off bulk crystal with the scotch-tape method, presenting an inexpensive method to fabricate high quality samples [26]. In contrast to QDs and color centers, 2D materials are optically active on the surface and can easily be integrated with on-chip technologies such as PICs [28]. Additionally, 2D materials such as the TMDs, can be epitaxially grown by chemical vapor deposition which could allow for precise placement of flakes, shown in figure 1.2. Therefore, fast fabrication and integration into PICs [27] can be realised with 2D materials. As such, SPEs in 2D materials show promise in the realisation of quantum photonic circuits, which has been a major bottleneck for QDs and color centers so far.

Due to these advantages of 2D material based SPEs, much research has been invested to determine how one can generate, control and tune their single photon emission. Much progress has been made and currently groups are starting to integrate 2D materials onto photonic waveguides: a first step towards on-chip quantum emitters [18].

While hBN-based SPEs can operate at room temperature due to a large band gap (6 eV) [24], electroluminescence is not easily achieved due to the large band gap. Electroluminescence is an important goal for on-chip SPEs, and is a method generally used with semiconductor devices. Therefore, in this work we focus on the semiconductor TMD material tungsten diselenide (WSe_2), which has a much smaller band gap of around 2.2 eV [29].

Ever since their discover, TMDs quickly received a lot of interest due to their exciting

optoelectronic properties. Especially interesting for optoelectronics and photonics are group-VI TMDs which exhibit bright photoluminescence (PL) [30] in monolayer form, due to their direct band gap [31].

Moreover, small screening effects in 2D materials lead to exceptionally strong Coulomb-bound electron-hole pairs, called excitons [32]. The creation and recombination of these excitons is an integral part in PL light emission, and important in order to understand single photon emission in these materials.

In TMD-based SPEs, excitons are trapped in local potential wells, before recombining by emitting a photon. These potential wells stem from localised strain [19] or defects such as atomic vacancies [33]. Moreover, tensile strain has been shown to decrease the band gap of TMDs [34], which can be used to create local energy minima. Using these properties, SPEs can deterministically be fabricated by placing flakes on an array of nanopillars [35]. However, the emission wavelength is still random and the precise microscopic origin of SPE in TMDs is not fully understood yet.

As such, SPEs in TMDs show promising future applications in quantum technologies. More research is however needed before the single photon emission quality has caught up with current solid state-based emitters.

In this work, we aimed to measure and characterise single photon emitters in WSe_2, where strain can be used to deterministically fabricate localised quantum emitters with high yield [35, 36]. To this end, a PL set-up was built from scratch for micro-photoluminescence spectrum, time-resolved PL and time correlation measurements. This set-up was then used to investigate mono- and fewlayer WSe_2 flakes placed onto nanometer-sized pillars. The results were analysed and compared with the theory to determine the nature of the PL emission.

In chapter 2, important theory pertaining to single photon emission in 2D-materials will be presented such as quantum optics, band structure and excitonic physics. Then, the theory of single photon emitters in TMDs and how they can be formed will be presented. Additionally, the characteristics that can be used to identify single photon emitters will be presented.

Chapter 3 will explain the experimental methods used to collect, filter and measure the PL emission from the samples. First, the components in the set-up will be explained, along with their uses and limitations. Then, the measurements used in this work will be explained, as well as what information is gained from these measurements.

Chapter 4 presents the results for characterisation of two samples, monolayer- and fewlayer WSe_2 flakes on nanopillars. Important aspects of the result will be discussed and explained by comparing to theory and recent research results.

Finally, in chapter 5, a conclusion of the results will be given and the future outlook of the project presented.

2

Theoretical background

In the first section of this chapter the knowledge necessary to understand the single photon state is presented. Following, a short introduction to the electronic band structure will be given which will connect with the theory of excitons in 2D materials. Finally, experimental data on SPEs in transition metal dichalcogenides will be presented and discussed.

The theory presented in this chapter will support the characterising and understanding of results obtained in this thesis.

2.1 Quantum optics

Most physical-optical experiments can be described sufficiently with classical theory of electromagnetism. However, in order to describe the second order coherence function quantum optics are required [37]. By quantising the electromagnetic field, the number states are introduced, which are used to describe the single photon state.

From the quantum optical description of the light states, conclusions can be drawn on the photon statistics behaviour that is expected. The statistical behaviour of these sources can then be used to differentiate between different states of light, such as chaotic light, coherent light and non-classical light.

2.1.1 Light states

In second quantisation of light the creation and annihilation operators, $\hat{a}^\dagger$ and $\hat{a}$ respectively, are used to describe light states. The energy ϵ_i of light in an electromagnetic mode i is expressed as

$$\epsilon_i = \hbar\omega_i(\hat{n}_i + \frac{1}{2}), \tag{2.1}$$

where ω_i is the frequency and $\hat{n}_i$ is the number operator given as

$$\hat{n}_i = \hat{a}_i^\dagger \hat{a}_i \tag{2.2}$$

The number state $|n_i\rangle$ describes light with a determined number of photons and is expressed as the eigenvector to the number operator [37]

$$\hat{n}_i \left|n_i\right\rangle = n_i \left|n_i\right\rangle , \tag{2.3}$$

where n_i is the number of photons in mode i. Number states are a type of non-classical light, only possible to describe by quantum mechanics.

The coherent states $|\alpha_i\rangle$, describe light with an indefinite number of photons and possess a high degree of optical coherence. Coherent states are eigenvectors of the annihilation operator and can be expressed as a superposition of number states [37]

$$\hat{a}_i \left|\alpha_i\right\rangle = \alpha_i \left|\alpha_i\right\rangle \ , \quad \left|\alpha_i\right\rangle = e^{-\frac{1}{2}|\alpha_i|^2} \sum_{n=0}^{\infty} \frac{\alpha_i^2}{\sqrt{n!}} \left|n_i\right\rangle , \tag{2.4}$$

where α_i is a complex eigenvalue. The most common example of a coherent light source is the laser.

2.1.2 Photon statistics

The degree of coherence is used to determine how much two electric fields correlate in time and space. In Young's double slit, light passing through two slits can interfere destructively and constructively, which is an example of spatial coherence. The first-order normalized coherence function is written as

$$g^{(1)}(x_1, x_2) = \frac{\langle E^*(x_1)E(x_2)\rangle}{\left[\langle |E(x_1)|^2\rangle \langle |E(x_2)|^2\rangle\right]^{1/2}}, \tag{2.5}$$

where $x_i = \{\vec{r}_i, t_i\}$ and $E(x_i)$ is the electric field. Using this function three types of coherence regimes can be defined as

$$\begin{aligned} \left|g^{(1)}(x_1, x_2)\right| &= 1, && \text{Complete coherence} \\ 0 < \left|g^{(1)}(x_1, x_2)\right| &< 1, && \text{Partial coherence} \\ \left|g^{(1)}(x_1, x_2)\right| &= 0, && \text{Complete incoherence.} \end{aligned} \tag{2.6}$$

The first-order coherence function is also called the amplitude-amplitude correlation function and correlates electric fields at different positions. However, it can be shown that both single photon sources and coherent light sources will give $g^{(1)} = 1$, because the first-order coherence function is unable to discern the photon number distribution of a light source. Therefore $g^{(1)}$ is not a suitable method to determine that a light source is non-classical.

Instead the second-order coherence function $g^{(2)}$ is used, also known as the intensity-intensity correlation function. As the name implies the second-order coherence function correlates intensity rather than electric field strength. The $g^{(2)}$ function is defined as

$$g^{(2)}(x_1, x_2) = \frac{\langle I(x_1)I(x_2)\rangle}{\langle I(x_1)\rangle\langle I(x_2)\rangle} = \frac{\langle E^*(x_1)E^*(x_2)E(x_2)E(x_1)\rangle}{\langle |E(x_1)|^2\rangle\langle |E(x_2)|^2\rangle} \tag{2.7}$$

If $\vec{r}_1 = \vec{r}_2$ in $x_i = \{\vec{r}_i, t_i\}$, then the equation can be simplified to

$$g^{(2)}(\tau) = \frac{\langle I(t)I(t+\tau)\rangle}{\langle I(t)\rangle^2} = \frac{\langle E^*(t)E^*(t+\tau)E(t+\tau)E(t)\rangle}{\langle E^*(t)E(t)\rangle^2} \tag{2.8}$$

Where $t_1 = t$ and $\tau = t_2 - t_1$ is the time difference between the two measurements. By utilising the quantum optical description an expression for $g^{(2)}(\tau)$ can be found which depend on the number operator [38], expressed as

$$g^{(2)}(\tau) = 1 + \frac{\langle(\Delta\hat{n})^2\rangle - \langle\hat{n}\rangle}{\langle\hat{n}\rangle^2} \tag{2.9}$$

We see that $g^{(2)}(\tau)$ is dependent on the difference between the variance $\langle(\Delta\hat{n})^2\rangle$ and the average $\langle\hat{n}\rangle$ photon number. For photon number distributions that follow a Poisson distribution like coherent laser light, the variance is equal to the mean and we get

$$g^{(2)}(\tau) = 1 \tag{2.10}$$

Which is to say that the intensity has no time dependence and is completely uncorrelated.

For a number state it can be shown that the $g^{(2)}(\tau)$ function at zero time delay is equal to [38]

$$g^{(2)}(0) = \begin{cases} 0, & n = 0, 1 \\ 1 - \frac{1}{n}, & n \geq 2, \end{cases} \tag{2.11}$$

which means that light has a low intensity correlation at zero time delay, which is called *photon antibunching*. For number states the variance is smaller than the mean and the distribution is thus called sub-Poisson. In figure 2.1 the distribution and the photon emission behaviour is shown for bunched, coherent and antibunched light sources. Only number states are able to show $g^{(2)}(\tau) < 1$ which makes the $g^{(2)}$ function a reliable method to determine the non-classical nature of light.

A SPE is a non-classical light source in a number state of $n = 1$, which is expected to yield $g^{(2)}(0) = 0$. With non-ideal sources other noise sources such as background light, dark counts and multi-photon emission can affect the measurement. Therefore, generally $g^{(2)}(0) < 0.5$ is sufficient to demonstrate that a light source is a SPE [39]. For $g^{(2)}(0) > 0.5$ the single photon state is no longer guaranteed as the two-photon state and higher could also produce such a result.

2.2 Electronic band structures

In order to understand mechanisms in semiconductor materials such as TMDs, a solid understanding of band structures is necessary. The band structure determines

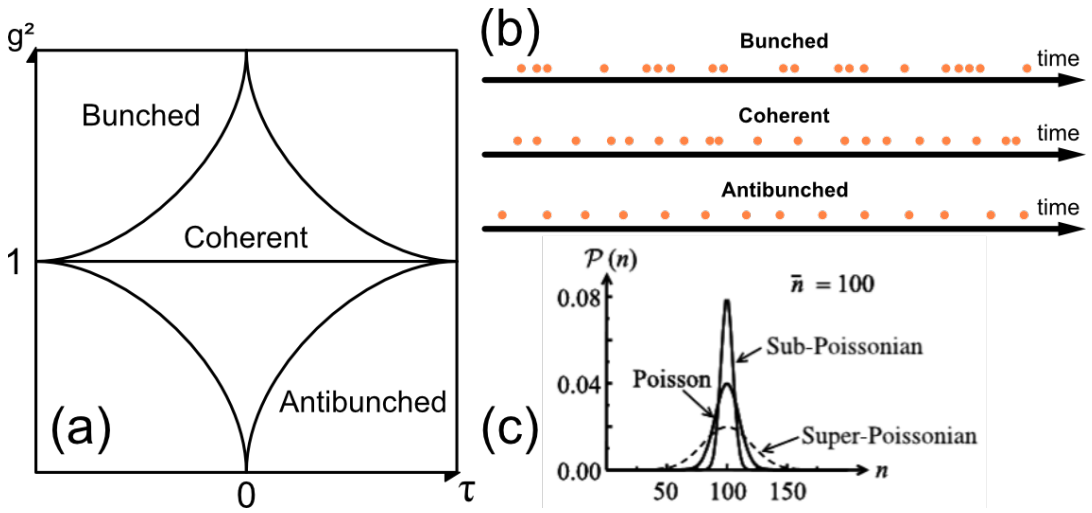

Figure 2.1: **a)** Schematic of $g^{(2)}$ result from bunched, coherent and antibunched light source. **b)** Photon emission pattern for bunched, coherent and antibunched light sources. **c)** The statistics of light with mean photon number $\hat{n} = 100$, for light with sub-Poisson, Poisson and super-Poisson distribution. Taken from ref. [40].

what energetic states an electron can occupy for different momenta. For large atomic systems such as crystals, the number of energy states is very large and will form a continuum of allowed states, called a band. In some cases a "forbidden" region with no allowed states is present, which is called a band gap.

Another important term to describe the electronic behaviour of materials is the Fermi level, E_F. When an energy state is at the Fermi level there is a 50 % probability that the state is occupied. The band below the Fermi energy is called the valence band (VB) and the band above the Fermi level is called the conduction band (CB). To find the probability that an electron occupies an energy level the Fermi-Dirac distribution function $f(E)$ is used, which is expressed as

$$f(E) = \frac{1}{1 + e^{\frac{E - E_F}{k_B T}}} \tag{2.12}$$

Where E is the energy, k_B is the Boltzmann constant and T is the temperature. At 0 K all states below the Fermi level are occupied and all states above are empty. If the Fermi level is located within a band then the material is a conductor, see figure 2.2. If the Fermi level is located in the band gap of a material then it is either called a semiconductor or an insulator. Typically materials with band gaps below 3 eV are called semiconductors and materials with larger band gaps are called insulators. In a semiconductor the electrons cannot move around in the filled VB and must be supplied with enough energy to overcome the band gap and get excited to the CB.

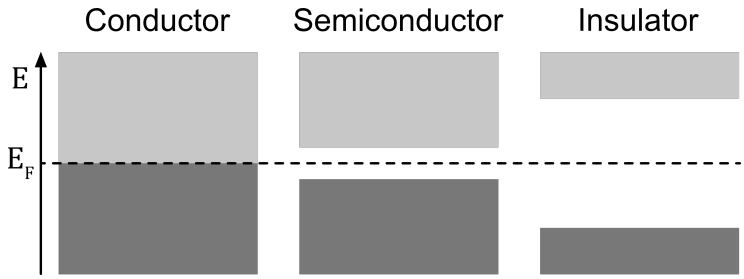

Figure 2.2: Electronic band structure of a metal, semiconductor and insulator at 0 K. Dark gray show occupied states while light gray show empty states.

The band structure can be calculated by solving the Schrödinger equation for the electronic wave function in a periodic lattice potential. The solutions give allowed energy levels that are functions of the momentum vector **k** for different band number λ. The energy solutions $E_\lambda(\mathbf{k})$ are periodic in k-space due to the periodic nature of the potential in a crystal lattice. The smallest repeatable unit cell in k-space is called the Brillouin zone (BZ) [41]. Solutions for the energy are usually plotted for symmetry points in the BZ, with an example for monolayer WSe_2 in figure 2.3a).

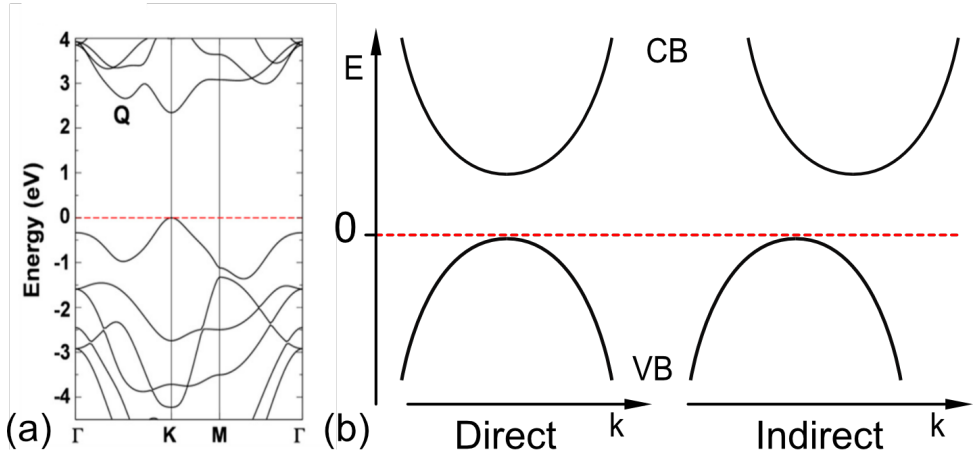

Figure 2.3: a) Example of a band structure for a monolayer WSe_2. On the x axis is momentum with important points of symmetry marked out. Taken from ref. [42] **b)** The difference of band structures for a direct and indirect bangap.

The band gap is defined by the energy difference between the valence band maximum (VBM) and the conduction band minimum (CBM) and can be either direct or indirect, see figure 2.3. In direct band gap materials the VBM and the CBM are aligned, with no momentum difference. Indirect band gap materials have a momentum difference between their VBM and CBM.

2.3 Excitons

When an electron is optically excited to the CB band of a semiconductor, a hole is left behind in the VB. The dynamics of the hole can be described mathemati-

cally similarly to an electron but with opposite charge. Excitons are quasi-particles which describe an electron and a hole bound together by Coulomb interaction. The electron-hole pair can be created by absorption of a photon, exciting an electron to the CB while leaving behind a hole. Exciton wavefunctions are describe by the Wannier equation expressed as [41]

$$-\Big[\frac{\hbar^2\nabla_r^2}{2m_r} + V(\mathbf{r})\Big]\psi_\lambda(\mathbf{r}) = E_\lambda\psi_\lambda(\mathbf{r}), \tag{2.13}$$

where $V(\mathbf{r})$ is the coulomb potential, ∇_r is the nabla operator, $\hbar$ is the reduced Plancks constant and m_r is the reduced mass. The reduced mass describe the effective inertia of the electron and the hole and is expressed as [43]

$$\frac{1}{m_r} = \frac{1}{m_e} + \frac{1}{m_h}, \tag{2.14}$$

where m_e and m_h are the effective masses of the electron and the hole respectively. Equation 2.13 is an eigenvalue problem where E_λ is the eigenenergy and the exciton wave function ψ_λ is the eigenfunction. The Wannier equation is similar to the hydrogen problem and can be solved for the bound-state energies with a similar result. The solutions for the binding energies of excitons in the bulk are [41]

$$E_b = -E_0\frac{1}{n^2}, \text{ with } n = 1, 2, ... \tag{2.15}$$

while the solutions for the binding energies in 2D flakes are

$$E_b = -E_0\frac{1}{(n+1/2)^2}, \text{ with } n = 0, 1, ... \tag{2.16}$$

Which follows a Rydberg series with the exciton Rydberg energy E_0 defined as

$$E_0 = \frac{e^4 m_r}{2\epsilon^2\hbar^2}, \tag{2.17}$$

where e is the electron charge, ϵ is the effective permittivity/dielectric constant [44]. Worth noting is that the binding energy for the ground state exciton is E_0 in bulk and $4\,E_0$ in 2D.

Additionally, the binding energy is inversely proportional to the square of the effective permittivity, which is related to the screening of Coulomb interactions. Because of the large area to volume ratio of 2D materials, excitons will be strongly affected by their surroundings.

As a result, excitons are strongly bound in 2D materials which yields smaller exciton radius. In the ground state, the exciton radius for bulk materials is a, while it is $a/2$ for 2D materials [41], where a is the exciton Bohr radius given by [44]

$$a = \frac{\hbar^2\epsilon}{e^2 m_r} \tag{2.18}$$

By binding together with Coulomb interaction to form an exciton, the energy of the electron-hole pair is lowered. The exciton energy is expressed by the equation

$$E_X = E_{BG} - E_b \tag{2.19}$$

where E_X is the energy of the exciton and E_{BG} is the energy of the free particle band gap [29]. The exciton states can be directly excited by light, creating optically accessible states in the band gap of semiconductors. The energy required to excite the ground state exciton from the VB is called the optical band gap. An example of a typical absorption spectrum of a 2D material with bound excitons is shown in figure 2.4.

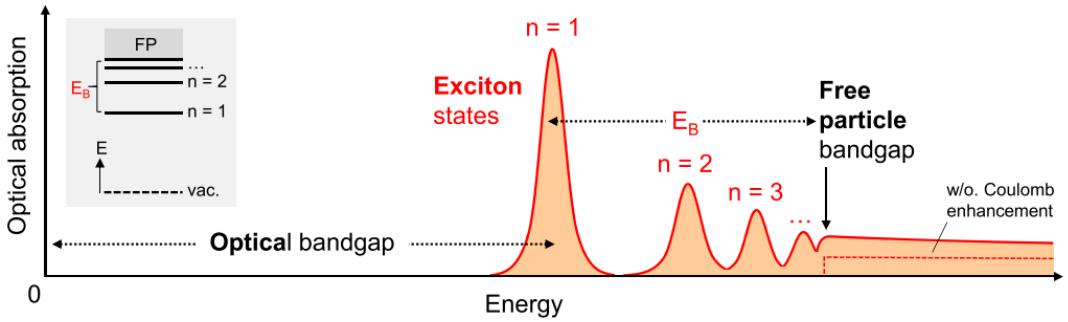

Figure 2.4: Optical band gap of a 2D material with the exciton binding energy order n marked out. Taken from ref. [29].

The ground state exciton has the strongest binding energy and will result in strong PL emission through exciton recombination.

2.4 Two dimensional transition metal dichalcogenide

2D materials are a large group of atomically thin materials. They are naturally found in bulk crystals, bound together by the van der Waals interaction. Due to their large area to volume ratio they are very susceptible to adsorbates [25] and their surroundings.

In this work we focus on TMD based 2D materials as they have been shown to yield interesting properties for quantum emitters. As semiconductors, electrical control of emission could be realised [45], which is important for on-chip integrated single photon sources.

Transition metal dichalcogenides are a group of 2D materials with a formula of MX_2 where M is a transition metal and X is a chalcogen atom. Bulk TMD can have a wide range of band structures ranging from semiconducting to metallic [31]. Especially interesting for optics are TMDs with Group-VI transition metals such as MoS_2, WS_2, $MoSe_2$ and WSe_2, which are direct band gap materials in monolayer form [46]. Moreover, TMDs have strongly bound excitons which enhances their PL emission. By introducing strain or defects these excitons can be trapped, creating localised emitters [35, 36]. These localised emitters have been shown to exhibit quantum

emission with $g^{(2)}(0) < 0.5$ [19–22, 47]. In the following section the details about PL emission in TMDs and recent findings will be explained further.

2.4.1 TMD band structures

TMDs are semiconductor materials with a trigonal prismatic (D_{3h}) unit cell, where transition metal atoms are sandwiched between chalcogen atoms. From a top down view they show an hexagonal structure similar to graphene and hexagonal boron nitride. In figure 2.5a) the structure of group VI-TMDs is shown.

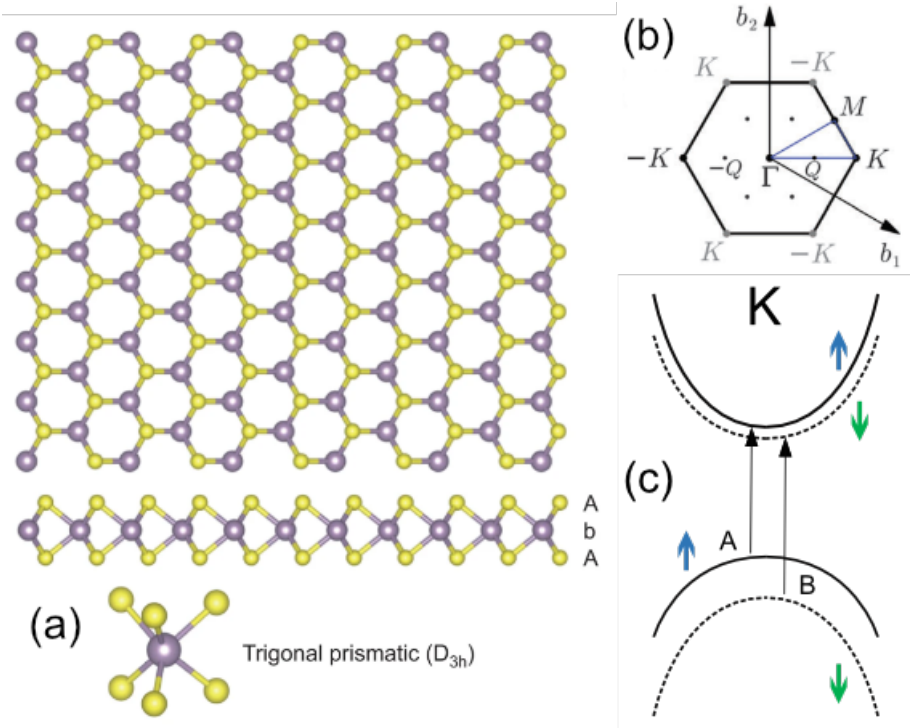

Figure 2.5: a) Top down and side view of single layer lattice of a TMD with the trigonal prismatic unit cell. Taken from ref. [31]. **b)** The first BZ with the reciprocal lattice vectors b_1 and b_2 is shown. Taken from ref. [48]. **c)** Illustrated band structure of WSe_2 at the K point of the BZ. CB and VB are spin split with spin up in solid line and spin down in dotted line. Shown are also transitions for the A and B exciton. The band structure at the -K point is the identical but with opposite spins.

By transforming the TMD lattice structure to k-space the hexagonal BZ is found, shown in figure 2.5b). Shown in the figure are symmetry points (Γ, K, M, Q) in the BZ as well as the lattice vectors b_1 and b_2. The band structure has translational symmetry along these lattice vectors.

In the corners of the hexagonal BZ we have the K and -K point, which have the same absolute momentum but differ by a phase factor. An electron can occupy either of the two valleys, which is called *valley-pseudospin*. In monolayer form, TMDs have a direct band gap at the K and -K points. The Γ point is the center of the BZ and has zero momentum. Shown is also the Q point which becomes the CBM in fewlayer WSe_2.

Both CB and VB experiences spin-splitting, where the energy for the spin up and spin down state are energetically separated. TMD CB mostly consists of d_{z^2} orbitals with zero angular momentum yielding a small spin splitting, around 40 meV for WSe_2 [29]. VB consists of $d_{x,y}$ and $d_{x^2-y^2}$ with an angular momentum of 2. A stronger spin splitting is therefore seen at VB, around 500 meV for WSe_2 [49]. Because electron transitions must be spin-conserving this creates two energetically different band gaps. The exciton created in the smaller band gap is called the A exciton while the larger band gap exciton is called the B exciton. In figure 2.5c) the spin splitting of the band structure at the -K point is shown along with the A and B exciton transitions. Because of the phase difference of the K and -K point, the spin splitting will be opposite for the two valleys.

The band structure is affected by the electronic landscape and as group-VI TMDs transition from monolayer to bulk, they transition from a direct band gap to an indirect band gap [50, 51]. In figure 2.6 the band structure for different thicknesses of WS_2 is shown with the smallest energy gap marked out. As WS_2 goes from mono- to quadlayer, the VBM changes from $K/\text{-}K$ to the Γ point. Additionally the CBM changes to the Q point and the new smallest transition is $\Gamma \rightarrow Q$. All group-VI TMDs have the same trigonal prismatic structure and follow a similar transition from indirect to direct band gap. The band gap of monolayer group VI-TMDs is around 50 % larger than the bulk band gap [31]. Because the orbitals that make up the Γ point (VB) and the Q points (CB) are mostly out of plane they are affected more by increasing layer thickness compared to the $K/\text{-}K$ points [29].

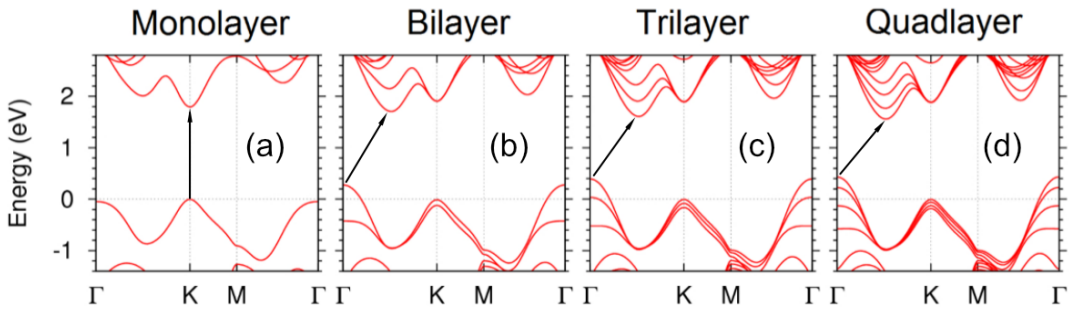

Figure 2.6: Calculated band structures of **a)** mono-, **b)** bi-, **c)** tri- and **d)** quadlayer WS_2. Solid arrows indicate the lowest energy transitions. Taken from ref. [52]

Another factor that will affect the band structure of TMDs beside thickness is the strain on the crystal. Strain on a material will change how much different orbitals overlap, which will affect the band structure. For WSe_2 monolayer it has been calculated that a compressive strain of around 1.5 % causes the band gap to go from direct to indirect, shown in figure 2.7. Moreover, a tensile strain causes the band gap to decrease energetically [34].

2.4.2 Optics in TMDs

PL emission comes from the radiative recombination of an electron and a hole with the emission of a photon. This transition must be spin- and momentum-allowed,

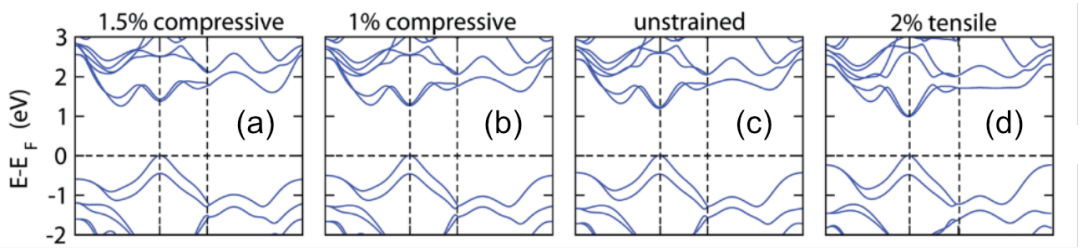

Figure 2.7: The band structure of monolayer WSe_2 depending on strain. Taken from ref. [34].

if this is the case, these excitons are called bright excitons. Spin- and momentum-forbidden transitions can however still occur if assisted by a phonon. The efficiency for these transitions is quite low and such excitons are called dark excitons. In figure 2.8 different excitons in WSe_2 are shown. Dark intra-valley transitions describe transitions within the same valley (K/-K) and conserve momentum but are spin-forbidden. Dark inter-valley transitions are transitions between different valleys and can be spin-allowed but are momentum-forbidden.

Since photons carry virtually no momentum, only momentum conserving transitions are considered bright. In figure 2.8 the momentum-dark indirect transition between the VB K point and CB Q points is shown as an example of a momentum-dark transition.

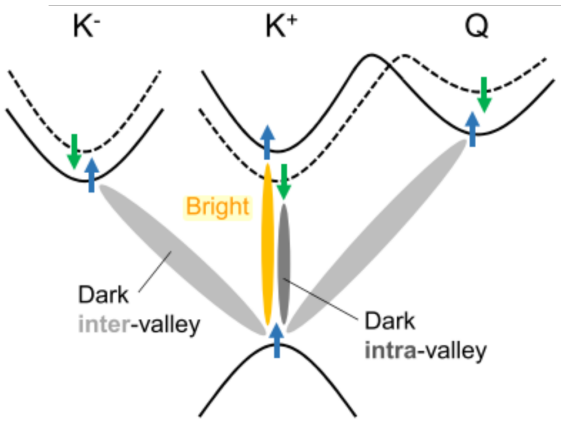

Figure 2.8: Bright and dark optical transitions in a TMD band structure. Taken from ref. [29].

After excitation to the CB, excitons will tend to relax down to the lowest energy state. In direct band gap materials this state supports momentum-conserving transitions, which yields stronger light emission. In figure 2.9a) the relative PL intensity is shown for different thicknesses of WSe_2. In the transition from mono- to bilayer, the PL intensity can be seen decreasing by more than a factor of ten. In figure 2.9b) the momentum-dark indirect exciton I emission peak decreases until it finally disappears as the thickness goes from bulk to monolayer.

With higher temperatures the phonon density increases, which increases the non-radiative relaxation channels. PL intensity is therefore expected to decrease at

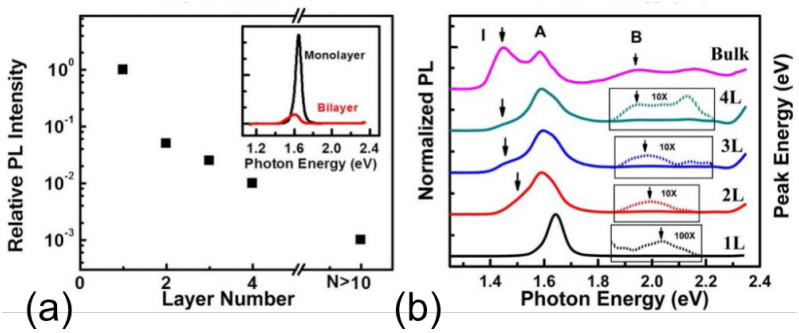

Figure 2.9: **a)** Integrated PL intensity by WSe_2 layer number. **b)** Normalized PL spectrum for varying thickness of WSe_2, with the indirect *I*, A and B exciton marked. Taken from ref. [52].

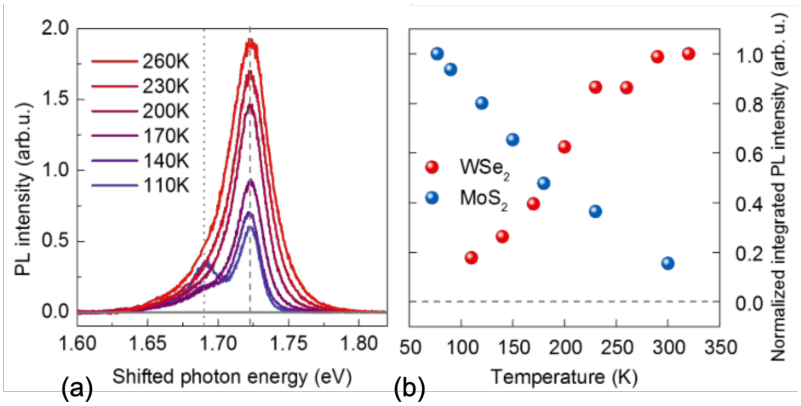

Figure 2.10: **a)** Temperature dependent PL intensity of monolayer WSe_2 with the peak shifted spectrally to overlap. **b)** Integrated PL intensity of WSe_2 and MoS_2 depending on temperature. Taken from ref. [53].

higher temperatures. Interestingly, the PL intensity for monolayer WSe_2 decreases at lower temperatures, shown in figure 2.10a). However, for monolayer MoS_2 flakes, decreased intensity at higher temperature is indeed observed, shown in figure 2.10b). An explanation for this is that the A exciton experiences quenching to the lower-lying spin-dark state [50] in WSe_2 at lower temperatures. As a result, a population of dark excitons are present at lower temperatures which could exhibit long lifetimes, due to absence of radiative recombination channels [53]. In MoS_2 the CBM state has a bright spin-allowed recombination channel [54] which can explain the opposing behaviour.

At lower temperatures other emission peaks than the A exciton also appear in WSe_2, such as the trion (exciton with an additional electron or hole) and the larger defect band with localised excitons seen in figure 2.11. In table 2.1 the typical emission peak energies for different excitonic transitions are shown.

Exciton	A exciton X^0	Trion $X^{\pm}$	Defect exciton X^D
Energy [eV]	1.75, ref. [19, 21, 22]	1.71, ref. [19, 21]	1.63, ref. [55]

Table 2.1: Typical peak energy at cryogenic temperature (∼10 K) for the neutral exciton, trion and localised defect states in monolayer WSe_2.

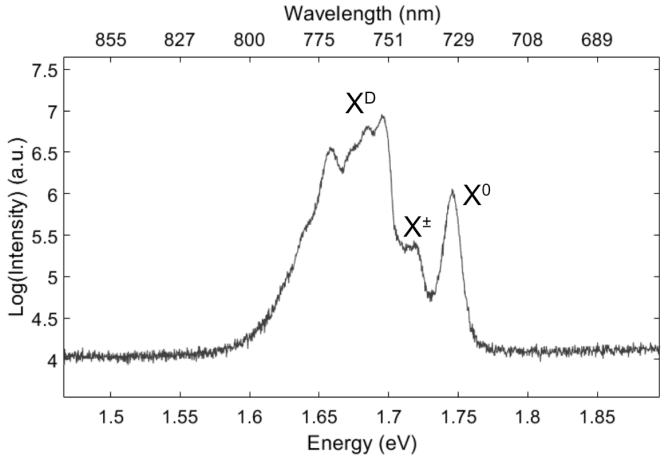

Figure 2.11: Low temperature PL emission from a monolayer WSe_2 flake measured in this work. In the figure the neutral X^0 exciton, trion $X^{\pm}$ and the defect band X^D are marked out.

The defect band is caused by localised point defects, to which the neutral A exciton diffuses and is trapped. Defects are naturally occurring in 2D materials and cause a broad band of emission. Because the defect band consists of localised excitons, the emission is expected to saturate at higher pump powers when the localised states are fully populated by excitons [55]. For exfoliated flakes of 2D materials with more than monolayer thickness there is also the momentum-dark indirect exciton X^I, which will have an emission energy heavily dependent on thickness of the flake as seen in figure 2.9b).

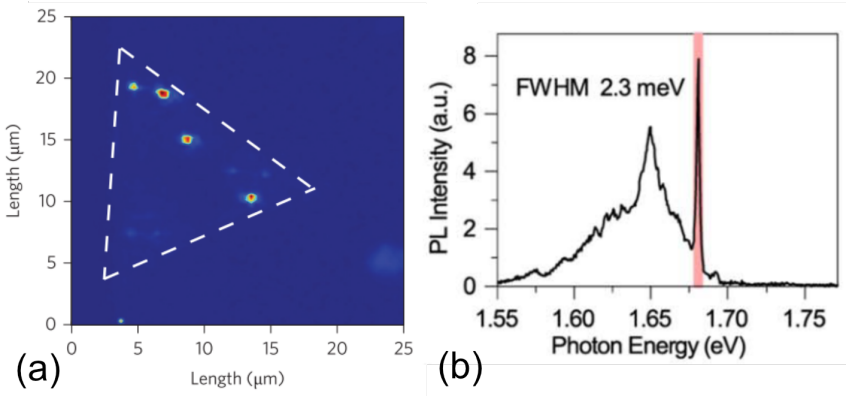

Figure 2.12: a) PL map of a monolayer WSe_2 flake with localised quantum emitters visible. Dotted line show the edge of the monolayer flakes. Taken from ref. [20] **b)** PL spectrum of a localised emitter on monolayer WSe_2 with a narrow emission peak marked out with FWHM linewidth of 2.3 meV. Taken from ref. [19]

Information about the efficiency of relaxation channels is found in the lifetime of the PL emission. After excitation the excitons first relaxes to lower lying states by thermalisation, which is a very fast process (500 fs) [56] after which they decay, radiatively or non-radiatively. For low temperatures the A exciton lifetime tends to be in the range of a few ps which increases up to a few ns at room temperature [57]. The longer lifetime has been attributed to intervalley scattering by phonons [58]. However, calculations have shown that the radiative lifetime of the A exciton at room temperature is expected to yield ns liftimes even without including phonon-scattering [57]. Additionally, a strongly non-resonant excitation high above the band gap will generate both intra- and intervalley excitons [29].

2.4.3 Single photon emitters

When exploring PL of WSe_2 spatially localised PL emitters were found at the edges of the WSe_2 monolayer flakes. In 2015 five independent groups were able to prove that these emitters were non-classical light sources [19–21, 23, 47]. This was done by spectrally filtering the emission from localised emitters and measuring the $g^{(2)}(\tau)$ function, yielding $g^{(2)}(0) < 0.5$.

At the location of these emitters the PL of the A exciton was found to be suppressed, which indicated that the emission came from quenching of the neutral exciton X^0 at these sites [19]. Because the emitters were found at the edges of the flakes the hypothesis was that strain or defects caused a localised quantum well, that trapped the A exciton. Figure 2.12a) shows an image of a PL map showing localised emitters on the flake. In figure 2.12b) the neutral exciton and trion is suppressed and a sharp high intensity peak can be seen. The emission peaks of these quantum emitters have a typical full width at half maximum (FWHM) linewidth around 0.1-2.3 meV [19,20]. As such, narrow linewidths appear to be a staple characteristics of SPEs.

These emitters typically show a lifetime in the range of a few ns at low temperatures [19, 20, 47, 54]. This is considerably longer than the A exciton lifetime and can be used to give indications of a localised emitter.

To test the strain dependence of the quantum emitters, WSe_2 flakes were placed on nanometer sized pillars to induce localised strain gradients. This was found to be an effective method of creating localised emitters seen in figure 2.13a). Once again narrow emission peaks were found that were confirmed to be quantum emitters by measuring the $g^{(2)}(\tau)$ function [35].

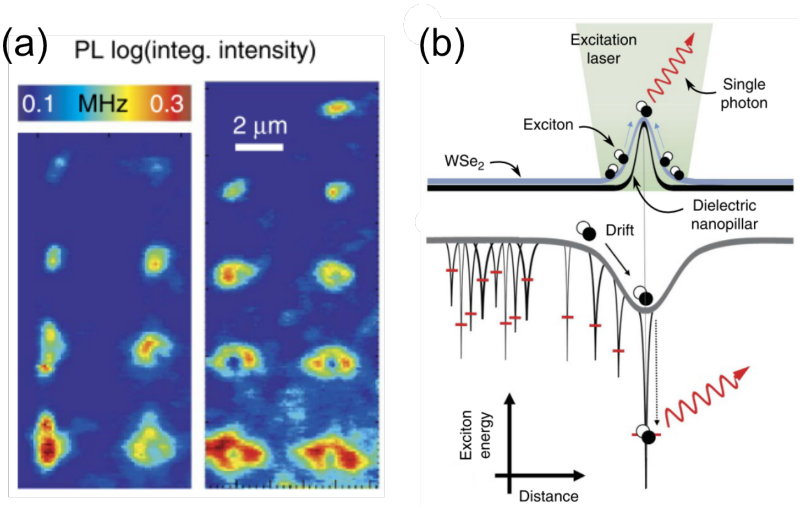

Figure 2.13: a) The PL map of a monolayer WSe_2 flake placed on top of pillars with increasing aspect ratio toward lower rows. Some emitters show a ring structure which is seen if the pillar pierces the monolayer. **b)** When the flake is strained by a nanopillar, a localised energy minimum will result. Many localised defect states are randomly distributed on the flake. As the excitons drift towards the localised energy minimum the defect state will trap excitons more efficiently. Taken from ref. [35].

2.4.4 Origin of the quantum emission

For quantum emitters, the exciton recombination path is closely tied to defect states present in the flake. These defects can be naturally occurring or introduced deterministically, e.g. with He-ion bombardment [33]. The defect introduces localised trapping states which can bind an electron or a hole.

A theory for the origin of these quantum emitters is illustrated in figure 2.13 b) and c). Because tensile strain decreases the band gap, an energy minimum will be created locally at the top of a pillar, where the strain is the largest. The excitons will drift to the energy minimum and get trapped in a local defect state and recombine. Due to the high exciton drift to the location, the defect state will be a highly efficient quantum emitter [35]. The drift of excitons to strained areas is called *exciton funneling* and is shown to be an effective method to generate strong PL emission. To generate a strong strain a high aspect ratio (height to width ratio of nanopillars) is better, but pillars can pierce the flakes if they are too sharp.

In TMDs the most common defect is the chalcogen vacancy [59], but in mechanically exfoliated and CVD grown WSe_2 flakes there is a high amount of W vacancies present as well [60]. From density functional theory (DFT) calculations for WSe_2,

these defects were shown to produce states in the band gap as seen in figure 2.14a) and b) [61].

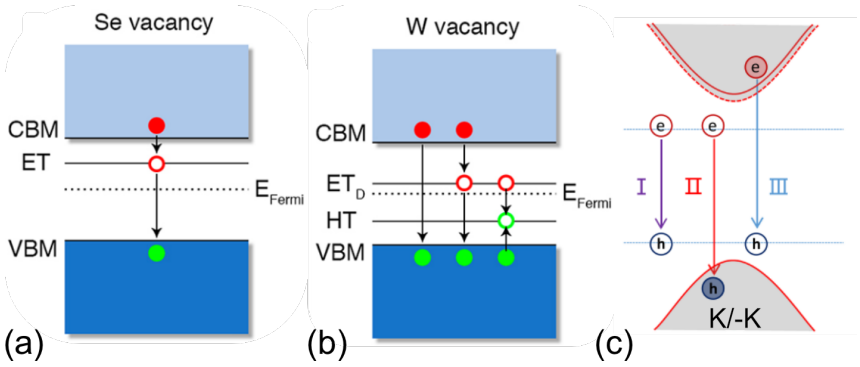

Figure 2.14: Schematic of recombination paths involving defect states. ET: Electron trapping, HT: Hole trapping. Open and filled circles show trapped and free states respectively. **a)** ET localised state present at a Se vacancy defect. **b)** ET and HT localised states present at a W vacancy defect. Taken from ref. [61].**c)** Three different recombination paths for defect excitons at the K/-K valley. In the VB a small spin-splitting is shown, with the spin-forbidden band shown with dotted lines. Shown are ET-HT assisted (I), ET assisted(II) and HT(III) assisted recombination. Taken from ref. [62]

Due to these extra trapping states three types of exciton recombination paths are possible, shown in figure 2.14c). Due to these states emission at lower energies than the optical band gap in pristine WSe_2 will be generated.

The recombination path of PL emission can be probed by applying a magnetic field and measuring the Zeeman shift (change in energy due to applied magnetic field). The magnetic moment of the exciton depends on the orbital magnetic moments of the VB, CB and defect states that the electron and hole occupy. Depending on the exciton magnetic moment a fine structure splitting will be generated at finite magnetic fields. The splitting for the three exciton recombination paths in figure 2.14c) is strong in ET assisted, moderate in ET-HT assisted and unobservable in HT assisted recombination [62]. Magnetic dependence will not be measured during this work, but is interesting for future applications.

Depending on the recombination transitions involved in the PL emission, different characteristics will be observed. Therefore, spectral wandering, saturation, lifetime behaviour could vary greatly even among emitters located in close proximity to one another.

3

Experimental Methods

In this chapter the experimental methods used to measure PL in WSe_2 flakes are presented. First, the working principle of the utilised instrumentation is explained as well as the working range and limitations. Then, the acquisition principle behind different measurements will be explained, as well as the information that these measurements yield.

In order to investigate emission in micrometer-sized flakes of WSe_2, optical excitation into the band is used to generate PL. Optical emission can be collected and the area of interest is spatially filtered with sub-micron resolution with a micro-photoluminescence set-up, explained in section 3.1. The emission spectrum is measured with a spectrometer at varying pump power, temperature and spectral wandering. From these measurements conclusions can be drawn on the PL emission such as saturation behaviour, ionisation energy and emission stability. Moreover, time-resolved PL measurements are used to measure lifetime and the $g^{(2)}(\tau)$ function, which is measured to obtain information on the nature of the emission.

3.1 Micro-photoluminescence set-up

Micro-photoluminescence microscopy is a common way to investigate optical behaviour of micrometer sized samples. Spatially resolved, high resolution PL measurements are commonly called micro-photoluminescence [63]. A simplified illustration of a micro-photoluminescence set-up is seen in figure 3.1.

When performing a measurement the sample is placed under a microscope and brought into focus. By focusing short wavelength light at the sample, electrons will be excited to the CB and can then relax down to the VB with the emission of light. The emission is collected by the microscope in the same path as the incident light. A beamsplitter (BS) or a dichroic mirror is used to pass the emission into a separate optical path than the excitation light. To isolate the PL emission from the excitation light a longpass filter is placed in the emission path, which will only allow light above a certain wavelength to pass. The measurement signal is spatially filtered to isolate PL from the area of interest. Spatial filtering can be achieved by coupling the light into an optical fiber or by placing a slit in the path of the emission.

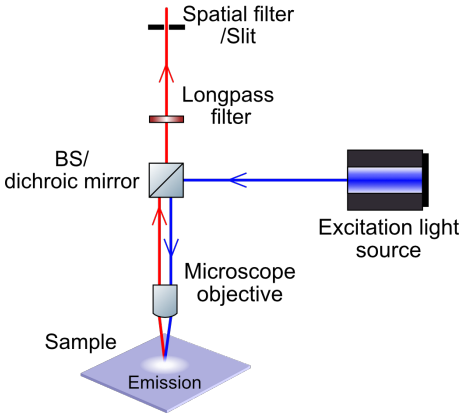

Figure 3.1: Micro-photoluminescence microscopy set-up. BS: beamsplitter.

3.1.1 Experimental set-up

The experimental set-up can broadly be divided into two parts: An excitation set-up and a measurement set-up, see figure 3.2. Here the working principles of each set-up is outlined and all important components are explained.

The excitation set-up has two functions: excitation and illumination. To locally excite the sample either a 730 nm or 485 nm laser can be used by flipping a swap-mirror. The laser light is then passed through an attenuator wheel, which can adjust the power of the light. After passing through some beamsplitters, the light is focused on the sample by a microscope objective located inside the cryostat.

Alternatively, a 470 nm LED located on a separate optical path can be used to weakly excite in a large area. The light is first filtered with a longpass filter to avoid any emission in the range of the sample PL spectrum as described in section 3.1.

To image the sample a 730 nm LED is used to illuminate the sample in a large area. The diffracted light is then collected with the microscope and passed to a camera, located on the same optical path as the 470 nm LED.

The PL emission is then passed through a longpass filter, before being collected to the measurement set-up by free-space or with optical fibers.

In the measurement set-up there are four major parts: the spectrometer, monochromator, life time set-up and Hanbury Brown & Twiss set-up.

With the spectrometer, sample emission collected by either free-space or optical fibers can be dispersed and measured with a charge-coupled device (CCD) to generate a PL spectrum. The spectrometer is the only part which uses the free-space collection, which is done for quick measurements and for PL mapping, explained in section 3.2.1.

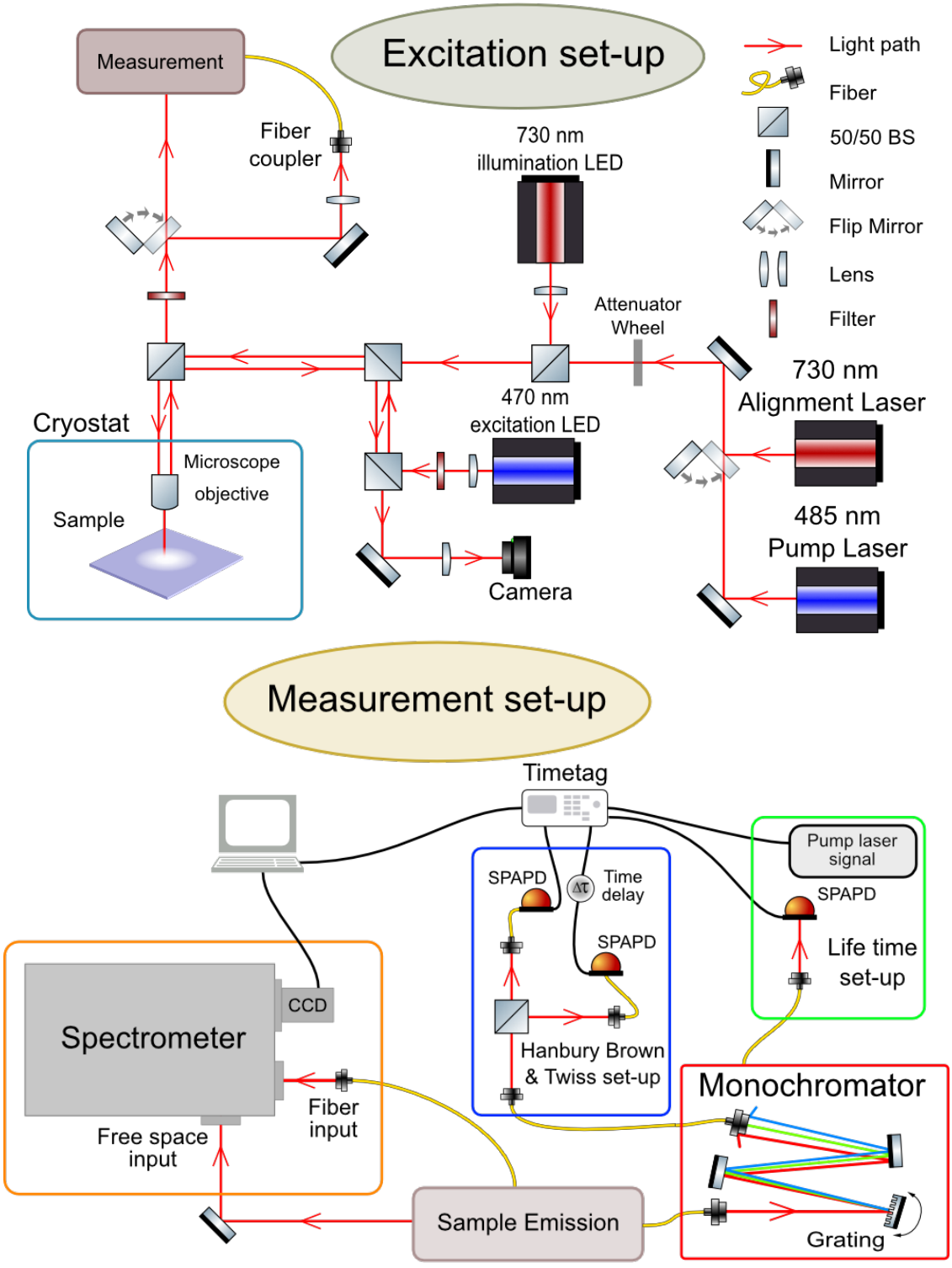

Figure 3.2: The measurement and excitation set-up used in the thesis work. Red lines show light paths, yellow are fiber connections and black are electronic signals.

The sample emission can also be passed through the monochromator, which will spectrally filter light at a certain wavelength. This is done by dispersing the light with a grating and then coupling a small spectral region into an optical fiber. To align on the correct wavelength, the output light is connected to the spectrometer

and measured. Then, light is sent to either the life time set-up or the Hanbury Brown & Twiss set-up for time correlation measurements, which is explained in detail in section 3.3.1 and 3.3.2 respectively.

The experimental set-up is built for flexibility, with the possibility to swap between different measurements without the need to align optics. Changing between different measurements is done by using flip mirrors and/or by changing fiber connections. The set-up is built on an optical table that is stabilised with pneumatic vibration isolators giving vibration levels below 5 nm.

Sample environment

Some measurements need to be done at low temperature and cooling to around 4 K is required. To achieve such temperatures while allowing for optical access a cryostat with windows is used. The cryostat is an AttoDRY800 mounted into an optical table.

The cryostat is a Gifford-McMahon cooler which uses high pressure helium gas in a closed-cycle system to cool a cold plate mounted through the optical table. The cold plate then cools the sample set-up, which includes a sample heater, sample holder, positioners and microscope objective mount, seen in figure 3.3. A thermal shroud is placed around the sample space as a radiation shield, and then a vacuum shroud is mounted on top to seal the system.

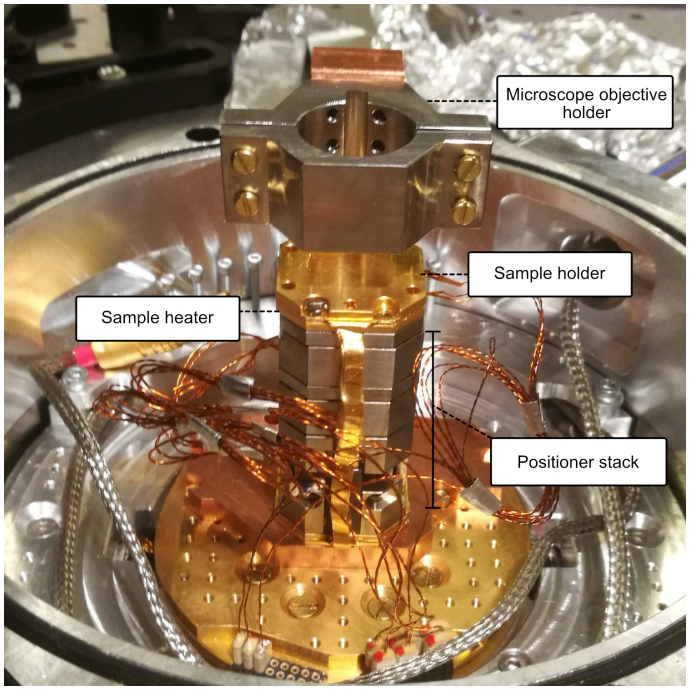

Figure 3.3: A picture of the sample stage used in the thesis work mounted on the cryostat without thermal shroud or vacuum shroud.

Vacuum is required to minimise heat transfer to the surrounding and also helps to preserve the sample from ambient atmosphere, which can lead to oxidation and adsorption of particles. The pressure is first brought down with a roughing pump

followed by a turbopump, with pressures reaching below 10^{-5} mbar at cryogenic temperatures.

To align the sample for measurements inside the cryostat, low temperature piezo nanopositioners are used. These are able to position the sample with micrometer resolution ($< 0.8\,\mu m$), but with some movement jitter ($1.2\,\mu m$).

The sample temperature can be controlled by the sample heater with a proportional-integral-derivative (PID) controller for temperature dependent measurements. Because the sample holder is in contact with the cold plate at 3.8 K, the maximum temperature that the sample can reach is around 120 K while the cryostat is in operation. Although, at higher temperatures the the heating rate slows down considerably.

Microscope objective

An optical microscope is used to view and collect emission from a sample with micrometer resolution. The microscope objective is a LT-APO/NIR/0.81, which uses several lenses to correct for chromatic aberrations, where light of different wavelengths is focused at different planes.

The effective wavelength range of an objective is the region where the focal shift δf is smaller than the field of focus Δ of a reference wavelength. Focal shift determines how far apart the focus point of light at different wavelengths are. Field of focus indicates how far an object can be moved from the lens's focus point while still giving a clear image. The field of focus is determined by the equation

$$\Delta = \frac{n\lambda_{ref}}{2NA^2} \tag{3.1}$$

Where λ_{ref} is the wavelength used to define the focal plane, NA is the numerical aperture and n is the refractive index of the medium (usually air). The focal shift of the microscope objective can be seen in figure 3.4 with depth of focus with $\lambda_{ref} = 930$ nm marked out. With a focus at 930 nm, the largest working range of 700-980 nm is achieved. Light at wavelengths outside from the optimal working range will be out of focus and appear blurry.

The magnification of a microscope is determined by the focal length of the microscope objective and the focal length of the tube lens to the camera by the equation

$$M = \frac{f_{tube\ lens}}{f_{objective}} \tag{3.2}$$

The focal length of the microscope objective is 2.93 mm which gives a magnification of 85x ($f_{tube\ lens} = 250$ mm) for the camera in the excitation set-up and 68x ($f_{tube\ lens} = 200$ mm) to the CCD in the spectrograph. These magnifications are sufficient to image and position the sample for PL measurments.

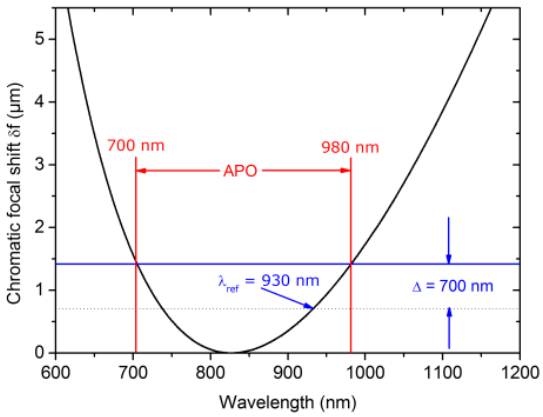

Figure 3.4: The focal shift δf of the microscope objective vs wavelength. Marked in red is the working range of the microscope objective where the focal shift is smaller than the depth of focus for light at 930 nm. Taken from ref. [64].

485 nm pump laser

To excite the sample a pump laser with emission wavelength around 485 nm is used, which consists of two parts: a Taiko PDL M1 laser driver with a LDH-IB-485-B laser head. The laser head can be operated in continuous wave (CW), pulsed and burst mode. However, in this work only CW and pulsed mode will be used.

The highest average power is achieved in CW mode with a maximum optical output power of 55 mW, compared to a maximum at 9.3 mW in pulse mode. The optical power in CW mode is constant over time, which is needed to read out information in power dependent measurements.

In pulse mode the sample is only excited in a short time window and then allowed to relax to the ground state, which is used for time correlation measurements. With each laser pulse, a synchronised output signal is sent from the laser driver to a time-to-digital converter (TDC), which logs the event, explained in detail in section 3.3. The synchronization output signal has a width of 5 ns and a falling edge signal delay around 10 ns with timing jitter smaller than 20 ps.

In order to measure lifetime of a sample it is important that the laser pulse is much shorter than the PL lifetime of the sample. In figure 3.5 a) and b) the pulse shape at 1.9 mW and 9.3 mW average power respectively is shown. At higher pump powers a second peak that last for around 1 ns can be seen. For lower pump powers the second peak is not as strong and a FWHM of 92 ps can be seen. Therefore, the laser should be operated with the lowest possible setting to shorten the pulse duration.

The laser head is coupled to a polarisation maintaining single mode fiber which introduces a coupling loss. The loss depends on the output power: At low power output the transmission is 8 % which increases to around 20 % at maximum power. However, according to the laser head specifications, a transmission at around 40 % should be expected for the fiber coupling and improvements should therefore be possible. The laser light has a linear polarisation which is conserved through the fiber.

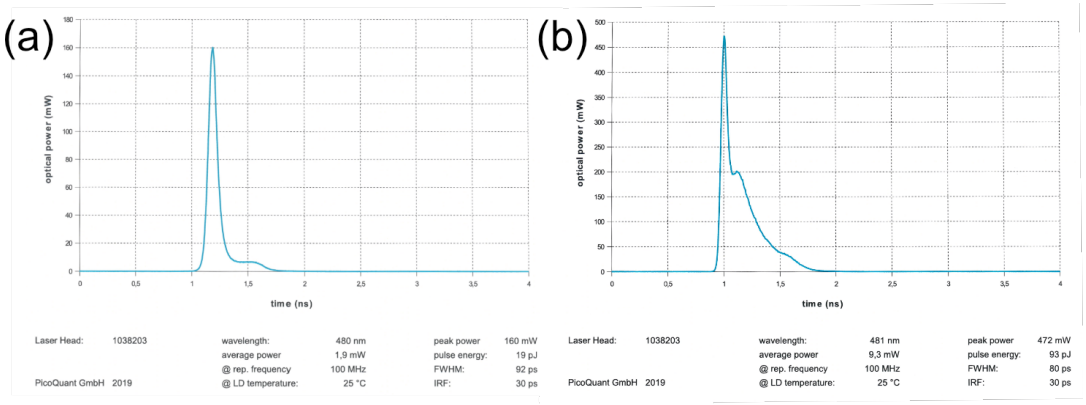

Figure 3.5: Pump laser time resolved emission in 100 MHz pulsed mode at **a)** 1.9 mW and **b)** 9.3 mW average power. LD: Laser diode, FWHM: Full width half maximum, IRF: Intrument response function. Taken from laser head data sheet provided by picoquant.

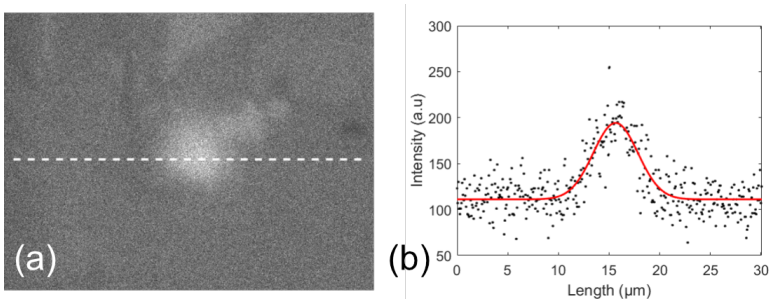

Figure 3.6: **a)** The blue channel from the image of the laser spot. Dotted line show the cross-section used for the gaussian fit. **b)** CCD pixel intensity on the cross-section with a gaussian fit giving a FWHM at $5.19^{+0.24}_{-0.21}$ µm with a 95 % confidence interval.)

The pump laser emits light with wavelengths far from the working range of the objective. As such, a large focal shift is unavoidable which results in a laser spot with FWHM around 5.19 µm in size, measured by fitting a gaussian distribution to images with the laser, shown in figure 3.6. Such a method yields a rough estimate, while a proper measurement would rely on measuring the beam diameter at and close to the focal position. Typical WSe_2 flakes are of comparable size to the laser spot, which makes local excitation impossible. As PL will be generated from a large area, extra importance is placed on proper spatial filtering.

730 nm alignment/excitation laser

A 730 nm laser is used to align the set-up and to excite the sample. The 730 nm laser is a LP730-SF15 laser diode with a CLD1010LP laser driver from Thorlabs. The laser is operated in CW mode with a maximum optical output power of 18 mW, with center wavelength at 729.1 nm and a linewidth around 1.4 nm (FWHM). The laser can easily be moved around the set-up by changing fiber connections.

As the 730 nm laser emits within the working range of the microscope objective,

it will focus properly on the sample, yielding a smaller laser spot. In this regard the 730 nm laser is better at local excitation compared to the 485 nm pump laser. However, 730 nm is equivalent to a photon energy of 1.7 eV and can therefore not excite into the free electron band of WSe_2 or the A exciton at around 1.75 eV. The laser can however excite into the defect band, although the excitation efficiency is expected to be lower.

Additionally, because the 730 nm laser wavelength is in the same range as the WSe_2 PL emission and filtering is no longer possible. Therefore the 730 nm laser is only usable for excitation when the emission of interest is energetically separated from the 730 nm laser. For the samples in this thesis the 730 nm laser is filtered from the PL emission with a 750 nm longpass filter.

730 nm illumination LED

To view the sample through the microscope objective it needs to be evenly illuminated. Because the microscope objective has a working range of 700 nm-980 nm, any light source with emission outside of that range will create a blurry image. Therefore a 730 nm LED was used to illuminate the sample, which results in a red tone of all sample images taken in the cryostat. An even illumination is achieved by focusing the LED in the conjugated focal point of the microscope objective. By doing this, a collimated illumination that covers the entire sample is produced.

470 nm excitation LED

We use a fiber coupled 470 nm LED at full power to excite the sample in a large area. As a result, weak PL will be generated which can be detected by the CCD in the measurement set-up for PL mapping, described in section 3.2.1.

The LED has a spectrally broad emission band, which overlaps with the emission range of the sample. Therefore, a 500 nm shortpass filter is placed in front of the LED fiber.

Attenuation

In the excitation set-up seen in figure 3.2, all light sources are aligned to the microscope objective in the cryostat. To align all light sources in one path many BSs are required. We use 50:50 BS throughout the set-up: 50 % of the light will be transmitted while 50 % of the light will be reflected. This means that the light will experience transmission loss throughout the set-up and be attenuated.

Attenuation is usually represented in optical density which is calculated by the equation

$$OD = -log_{10}(t) \tag{3.3}$$

Where t is the intensity transmittance of light in the optical component. OD is useful as the value for each optical element along a path is added together for the total attentuation. Listed in table 3.1 are the OD values for the components with the largest transmission losses in the set-up. The 485 nm pump laser experiences

most attenuation to the microscope objective with an OD between 1.64 - 4.0, which translates to a transmittance of 0.01 - 2.3 %, mostly due to the fiber coupling losses mentioned before.

Because the samples can have weak emission it is important to not attenuate the signal before measurements. The two components that can be changed to improve transmission in the collection path is the 50:50 BS and the SPAPD. By changing the 50:50 BS to a 90:10 BS a 40 % increase in transmission can be achieved. A lower reflectivity would however further attenuate excitation and illumination light. As a result PL mapping and imaging of the sample could prove to be difficult.

Component	OD
50/50 BS	0.3
Attenuator wheel	0.04 - 2
485 nm pump laser fiber coupling	0.7 - 1.1
Collection fiber coupling	0.35
Grating system	0.25
Spectrograph	0.7 - ∞
Single photon detectors	0.60-0.92

Table 3.1: Optical density of relevant components in the excitation set-up.

Optical fiber

The fiber collection can be used to spatially filter the PL emission as it is only possible to couple the emission from a small spatial spot into the fiber core. There are two options when choosing fibers: single mode and multi mode fiber. Single mode fiber have a smaller core of around 9 µm which only allows for one transversal mode. Multi-mode fiber has a larger fiber core around 50 µm and supports several transversal modes. Coupling to multi-mode fiber will result in less loss but with a broader spectral linewidth and lower resolution.

Spectrometer

The spectrograph used is a Shamrock 500i with two inputs, one for free space input and one for fiber input. The free space input is mounted with a motorised slit with a range of 10 - 1000 µm. The slit can be used to spatially filter part of the emission from the sample. Inside the spectrograph there is a Czerny–Turner monochromator set-up which is illustrated in figure 3.7.

A spectrograph is used to disperse light into its electromagnetic spectrum to measure the wavelength dependent intensity. The light is dispersed by a blazed grating, which diffracts light into it spectral components. Blazing on a grating is a surface structure that optimises efficiency for certain wavelengths, called the *blaze wavelength*.

After the light is diffracted, its spectrum will be spread out in space and part of the spectrum will be measured on a CCD. The size of the spread is determined by the number of lines per millimeter (l/mm) of the grating. A higher number of l/mm results in a broad spread and yields a higher resolution.

To change what spectral range is measured on the CCD, the angle of the diffraction grating can be adjusted. Inside the spectrograph a grating turret which holds three different blazed gratings is mounted. In table 3.2 the l/mm and blaze of these gratings is shown. The grating turret will then rotate to change the center wavelength and to swap the grating. Moreover, the grating can be aligned to operate as a normal mirror, which is used to image the sample on the CCD for PL mapping or to align the set-up. To image the sample, free space input needs to be used.

Grating turret	l/mm	Blaze
Grating 1	300	500
Grating 2	600	500
Grating 3	1200	500

Table 3.2: Gratings used in the spectrograph grating turret.

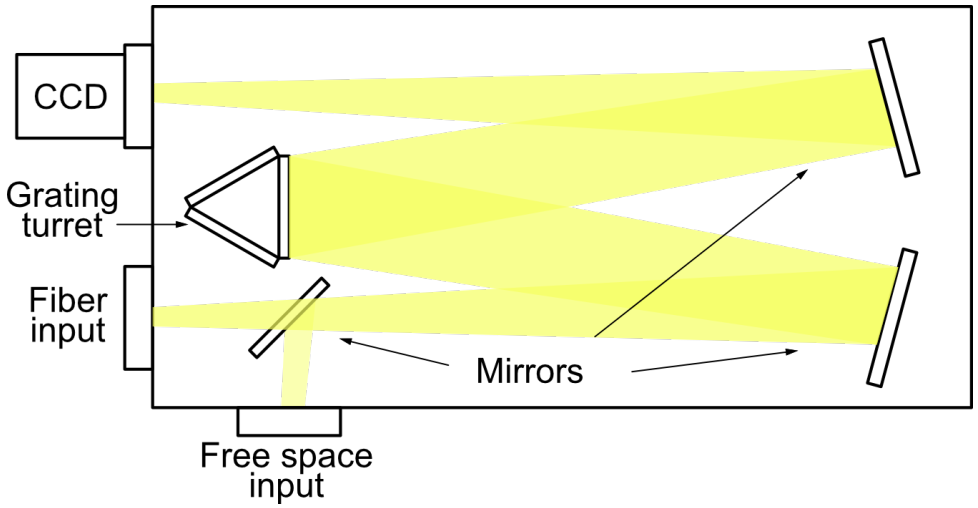

Figure 3.7: An illustrative figure of the inside of a Czerny–Turner spectrograph with light paths in yellow.

Charge-coupled device

To measure the intensity of the emission with high sensitivity a CCD is used. The CCD used here is an iDus 416 with a sensor size of 30 x 3.8 mm with 2000 x 256 pixels. As the pixel of a CCD absorb light they will accumulate electric charge proportionally to the intensity. After exposure is finished the electric charge of each pixel will be read out. Additionally some counts will be spontaneously generated in each pixel which is called the dark noise. To decrease dark noise the CCD is thermoelectrically cooled down to $-80\,°C$. At this temperature the dark count is 0.007 e^-/pixel/s compared to RT where the dark count is well above 1000 e^-/pixel/s. Thanks to this low noise level, even emission from weak sample emission can be measured. For these samples however, a longer exposure time is needed in order to accumulate counts for a clear signal.

The CCD can also log data in kinetic mode, where multiple frames are taken in succession, which is useful for time dependent measurements.

The quantum efficiency of the CCD depends on the wavelength with a maximum of 95 % at 800 nm. Currently, the spectral dependence of the CCD and the grating is not adjusted for. Therefore the intensity counts measured in the spectrograph do not accurately reflect actual counts. Over shorter spectrum ranges however, the efficiency is not expected to change significantly and the relative intensity of emission peaks can be compared. In the future, a source with known emission spectra could be used to correct for spectral efficiency dependence, yielding accurate counts.

Because the measurements are very sensitive to background light, all non essential light sources are turned off in the lab. Additionally a background spectrum is taken for each measurement, which is then subtracted from the PL spectrum data.

3.2 Typical sample characterisation measurements

In this section the various measurements used to characterise and analyse the sample PL is presented. First, the method used to acquire each measurement is described and the information it can generate is explained. Additionally, equations used to fit data is presented and motivated.

3.2.1 Photoluminescence mapping

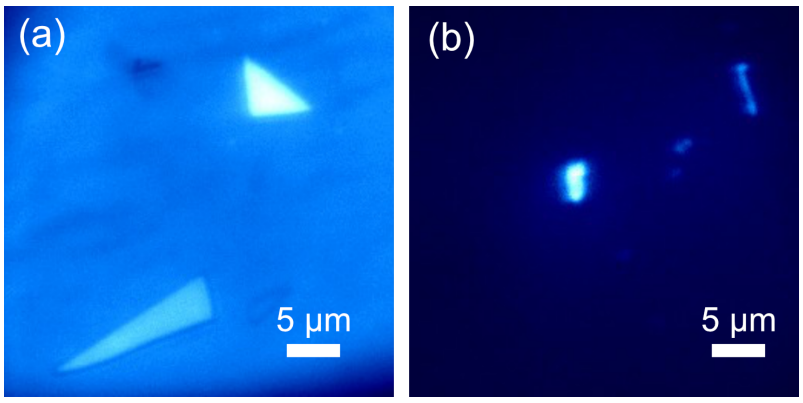

Figure 3.8: The image and PL map of a monolayer flake generated on the CCD. **a)** Image of a monolayer WSe_2 flake taken with the spectrograph CCD, illuminated by a 730 nm LED at low power. The monolayer is not visible due to the thickness. **b)** PL map of a monolayer WSe_2 flake taken with the spectrograph CCD, excited by a 470 nm LED at maximum power. The photoluminescent monolayer is visible, while the optically inactive surrounding are not visible.

Emitters will exhibit stronger PL compared to the surrounding. To quickly find the position of these emitters a PL map can be generated. This is done by exciting a large area and then imaging the PL emission onto the CCD. Excitation is done with

the 470 nm LED at full power. In figure 3.8 an example of a sample imaged on the CCD is seen with 730 nm LED illumination in a) and 470 nm LED excitation in b). With the 730 nm LED everything is illuminated and a few layer is visible along with a coordination marker on the chip. The monolayer is however too thin and is not visible. When the 470 nm LED is used only the emission at higher wavelengths is visible because of the 550 nm longpass filter.

After getting the PL map the location of emission on the sample must be identified. The 730 nm LED is used at low power to image the sample on the CCD. The image is then overlapped with the PL map generated. In figure 3.8 the image and PL map of a WSe_2 monolayer is seen, together they give information about the location of emission on a sample. If the intensity of the emitter is strong enough it is possible to image the sample and the PL map at the same time.

3.2.2 Power dependence measurement

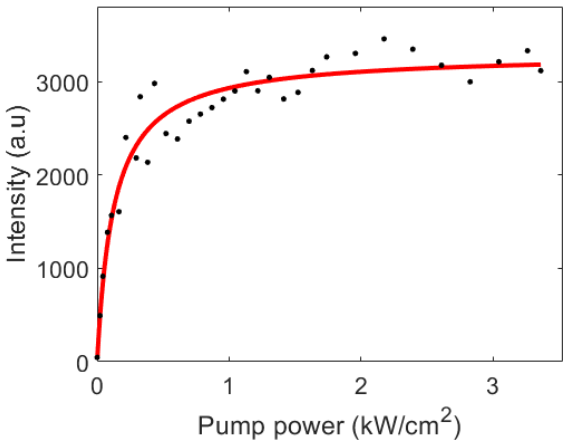

Figure 3.9: Example of power dependence measurement of a defect emission peak with a saturation behaviour fitted function. From the fit a saturation power density at 137 W cm^{-2}.

To determine the power dependence of the emitters, the sample is excited with CW laser light. CW mode is used for a constant power output over time, which is easier to model saturation behaviour to. The attenuator wheel is used to vary the laser power which is measured with a power metre before the cryostat. For each power a PL spectrum is taken, from which emission peaks can be found. The intensity is summed over a spectral range, which gives the total emission for that range. By choosing the spectral range where emission peaks are found, their data can be isolated from the rest of the emission. The total intensity of that spectral range can then be plotted as a function of power density.

Localised emitters can not be excited indefinitely and are at some power density expected to show saturation behaviour, which can be modeled by the equation [22]

$$I = I_{sat} \cdot \frac{P}{P + P_{sat}}, \tag{3.4}$$

where I is the emission intensity, I_{sat} the emission intensity at saturation, P the power density and P_{sat} the saturation power density where $I(P) = I_{sat}/2$. In figure 3.9 an example plot is shown with a fitted function.

3.2.3 Temperature dependent measurement

In figure 3.10 a typical temperature dependent measurements is seen for a monolayer WSe_2 flake. The behaviour of different peaks can be followed as the temperature is changed. In this example the neutral exciton at 1.74 eV is seen red-shifting slightly at higher temperature. Meanwhile, the broad defect band, at 1.66 eV decreases in intensity as temperature increases.

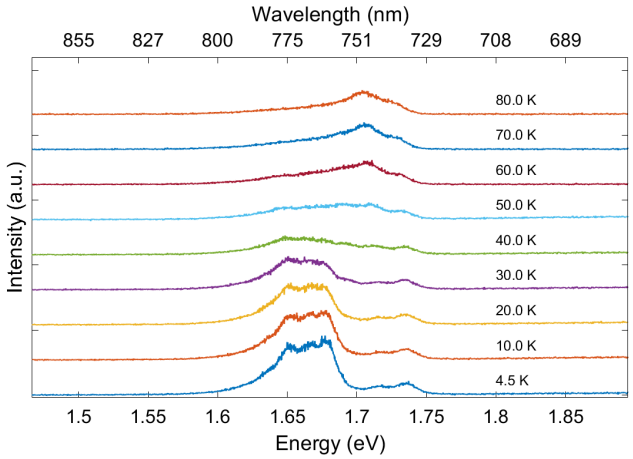

Figure 3.10: Example of a temperature dependence PL spectrum of a monolayer WSe_2 flake.

At lower temperatures phonon occupation will decrease together with non-radiative decay, which yields a higher PL emission intensity. Excitons are also trapped in localised states and defect emission is increases. When the characteristic energy is higher than the ionisation energy of the trap, excitons will escape and the trapping efficiency decreases. The ionisation energy E_a can be calculated by measuring the maximum intensity of an emission peak for each temperature and fitting the data to the equation [65]

$$I(T) = I_0 \cdot e^{-\frac{k_B T}{E_a}}, \tag{3.5}$$

where I is the intensity, I_0 the intensity at 0 K, T is temperature and k_B is the Boltzmann constant. The temperature dependence can give valuable information about carrier dynamics of the different emission peaks in a sample.

After cooling the sample to 4.5 K the sample heater is used in PID control to heat the flake to the desired temperature. The temperature sensor is placed on the

sample holder and the sample must be allowed to thermalise for an additional period after the settling time of the PID control. A PL spectrum is then taken with the laser in either CW or pulsed mode. The laser will also heat the sample, with a rate proportional to the optical input power. If PL measurements are taken at different power inputs the sample needs to thermalise for a short period between each measurement. After a measurement has been taken the temperature is changed for a new measurement and the sample is allowed to thermalise again. Because heating causes material expansion the focus and position of the sample can change and needs to be adjusted between measurements.

3.2.4 Polarisation dependent measurement

Depending on the nature of the emitter the emitted light will have different polarisation, which is investigated by polarisation dependent measurements. The PL emission is passed through a linear polarising filter placed in a rotational mount and the angle of the rotational mount is logged. After measuring the filtered PL spectrum with the spectrograph the measurement is repeated with a new angle of the linear polarising filter. The wavelength emission intensity dependence on the

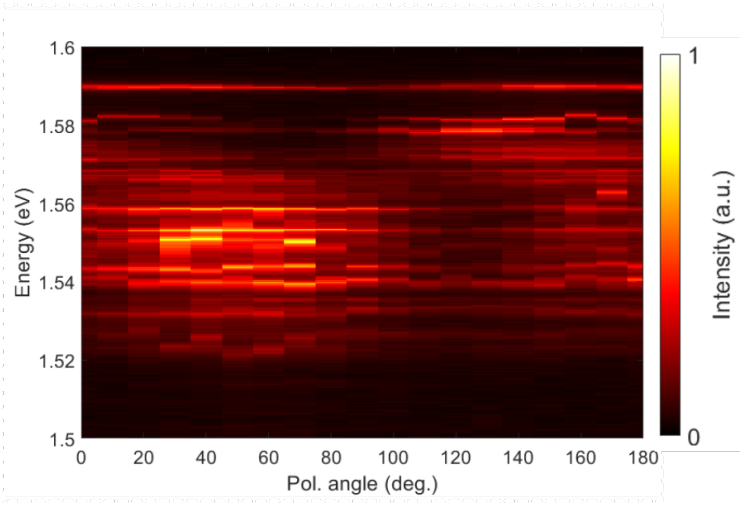

Figure 3.11: Example of polarisation dependent measurement.

polarisation angle is then plotted, seen in figure 3.11. The plot shows periodic behaviour for different emission peaks, with information about the polarisation of the emitters.

3.2.5 High resolution spectral filter

To spectrally filter emission peaks of interest a monochromator is used. The monochromator has a similar set-up as the internal optics of the spectrograph. The light is diffracted on a 1200 l/mm grating with 750 nm blaze wavelength and then collected by a fiber. The grating set-up used with a 785 nm SM fiber has an efficiency of around 45 % at 800 nm with a linewidth of around 0.22 nm, seen in figure 3.12.

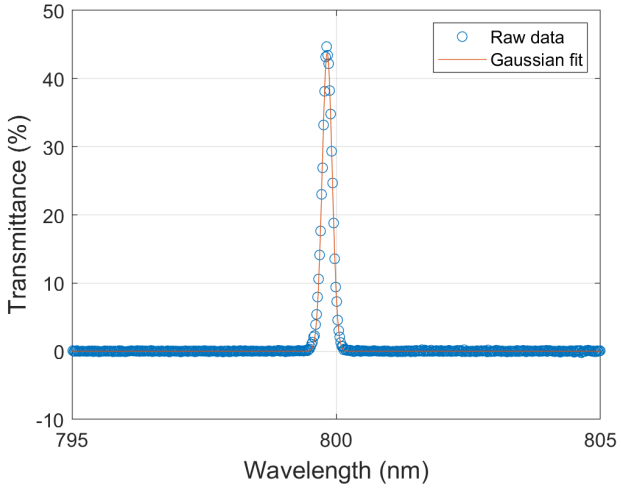

Figure 3.12: Measured transmittance of white light source through the monochromator set at 800 nm. The fitted FWHM is 0.22 nm.

When using the grating system it needs to be aligned on the correct wavelength. To do this a white light source is diffracted and its spectrum is then analysed in the spectrograph. The center wavelength can then be aligned by rotating the grating. After the grating system is aligned the input fiber is changed to the sample emission.

3.3 Time correlation measurement

To understand the nature of emission, the mechanisms of recombination are important to understand. Time correlation measurements are used to probe how the PL emission is created and then emitted. The time scale for emission can then be compared to theoretical calculations to explain what recombination path might be taking place. In the following section the measurements methods and important components will be presented.

We use time resolved photoluminescence (TRPL) set-up to investigate the life time of emitters. Additionally the $g^{(2)}$ function is measured with a Hanbury Brown & Twiss set-up to determine the nature of the emitters [66].

For time correlation measurements two components are important: A detector with high timing accuracy and a time-to-digital converter (TDC).

Single photon avalanche diode

The detectors used in this project are fiber coupled single photon avalanche photodiodes (SPAPD) from MPDs PDM series. With these emitters light can be detected with single photon resolution and have a timing accuracy around 35 ps, which is very low. The quantum efficiency is wavelength dependent and is shown in figure 3.13, for fiber coupled and free space detectors. In the expected emission range of WSe_2 (700 - 800 nm), the quantum efficiency (QE) is between 12 - 25 %.

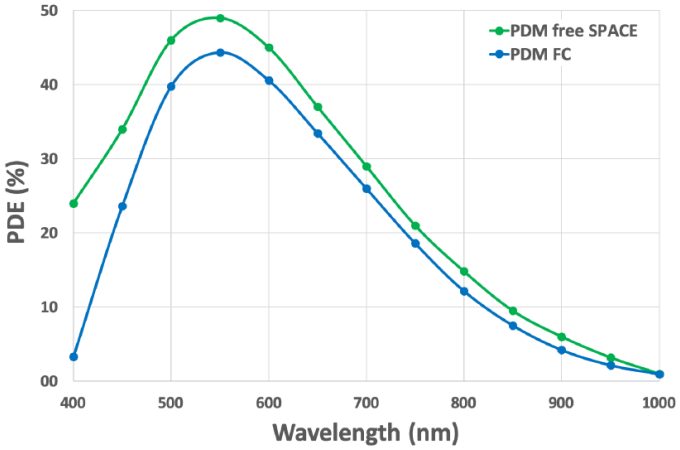

Figure 3.13: Quantum efficiency of the PDM series SPAPD at different wavelengths. Fiber coupled set-up in blue and free space set-up in green. Taken from ref. [67].

Some signals will be generated due to dark counts in the SPAPDs, which is 18.7 and 17.3 counts/s for the two detectors and is considered to be low for single photon detectors. To measure a sample the signal-to-noise ratio should be as high as possible to avoid washing out the signal.

Time-to-digital converter

The TDC will take electrical signals from different channels, correlate them in time and log the data. The data logging is done by assigning a start and a stop channel. After a start signal has been registered a counter will begin. For each following stop signal, the time delay from the start will then be logged, illustrated in figure 3.14. In this work a TDC named quTAG from qutools is used with a digital resolution of

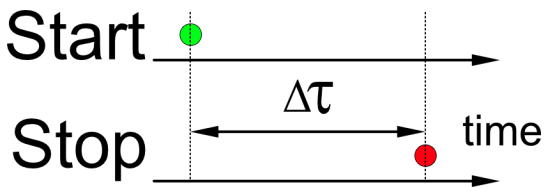

Figure 3.14: Illustration of how a measurements is logged in the TDC set-up.

1 ps. In the set-up there can be a signal delay between channels, for example caused by a difference in cable lengths or by equipment delay. To account for this a delay time can be applied to different channels digitally.

Additionally, a digital dead time can be set to a channel, where no new signal will be registered for a period. The quTAG in use has a natural dead time of 40 ns, which is lower than the SPAPDs (≈75 ns). Any noise that triggers a signal in the quTAG during the detectors dead time should and can therefore be ignored with this option.

3.3.1 Time resolved photoluminescence set-up

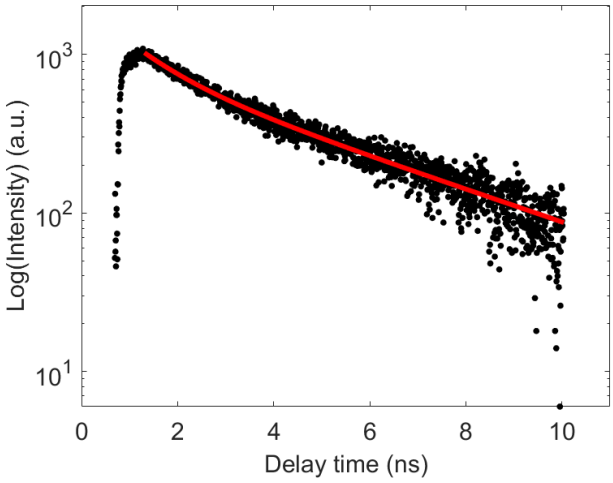

Figure 3.15: Example of a lifetime measurement fitted with a biexponential function.

In TRPL measurements the electrical signals will be collected from the laser driver with each pulse and the from the SPAPD for each photo-detection event. First, the pulsed laser will periodically excite the sample and at the same time send a start signal to the TDC. The PL emission from the sample will then be collected and sent to the SPAPD, which will generate the stop signal.

In TRPL, the TDC will be operated in multi-stop mode, which means that all stop events after a start will be logged. The time delay for each photo-detection event can then be plotted in a histogram, see figure 3.15.

The PL emission decay over time can be modeled by exponential functions and fitted to the equation

$$I(t) = C \cdot e^{-\frac{t}{\tau}} + I_{bg} \tag{3.6}$$

Where C is a constant, t time, τ the lifetime of PL emission and I_{bg} is background counts arising from the ambient light or dark counts of the SPAPDs. The lifetime give information about the different relaxation processes of the carriers.

The accuracy of the lifetime measurement is affected by the timing resolution of the detectors and the laser driver. Additionally, the laser pulse shape and the instrument response function (IRF) will affect the measurements and limit the resolution. The IRF gives information on how the pulse width is changed when passing through the set-up. In order to measure the IRF a laser pulse is sent through the set-up and the time-resolved pulse shape is measured. In our work the limiting component is the laser pulse width of 92 ps.

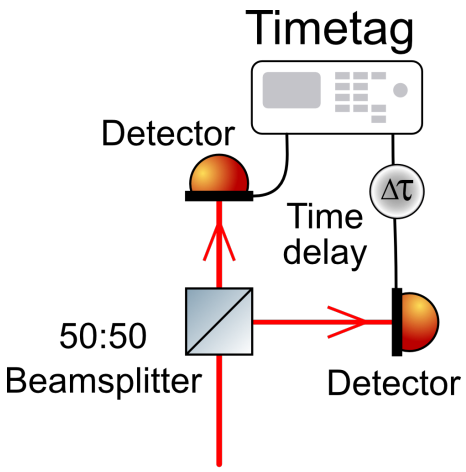

Figure 3.16: Hanbury Brown & Twiss set-up. BS: beamsplitter, SPAPD: Single photon avalanche diode, τ: time delay.

3.3.2 Hanbury Brown & Twiss set-up

To measure the $g^{(2)}$ function, the most common way is to use the Hanbury Brown & Twiss (HBT) set-up. The light is split in two paths with separate detectors by a 50:50 BS, and the signals generated are sent to a TDC. An illustration of the HBT set-up is seen in figure 3.16.

For the HBT measurements, one of the SPAPDs is designated as the start signal and the other as stop. A digital delay is applied to the stop channels in order to also record negative delay differences. If both channels receive a signal within a set time period of each other, the event is then logged with the time difference. This time difference is then plotted in a histogram and normalised.

If the light source is a single photon source it will show antibunching behaviour and two detectors can never generate a signal at the same time. As a result a dip below one is seen for zero time delay, previously illustrated in figure 2.1 in chapter 2.

3.4 Sample fabrication

Fabrication of 2D material monolayers is straight forward, but must be done with great care. Because 2D materials are very sensitive to adsorbates it is important to keep the samples in a clean and isolated environment. Fabrication is done in a clean room with ISO class 4-5 and the sample is stored in a vacuum sealed bag between uses.

The flakes are transferred onto a prefabricated SiO_2/Si chip with a SiO_2 thickness of 285 nm. The silicon chip comes marked with coordinate markers so that the flake can be located.

3.4.1 Mechanical exfoliation

The samples were fabricated by mechanical exfoliation (scotch tape method) of bulk crystals [26]. Nitto tape is used to peel of flakes from the crystal. The flakes are then peeled repeatedly by bringing two pieces of tape together and separating them. This will yield flakes with random distribution of thickness and shape, with some monolayers and bilayers. The flakes are then deposited either directly on the chip or prepared for dry transfer technique.

3.4.2 Dry transfer technique

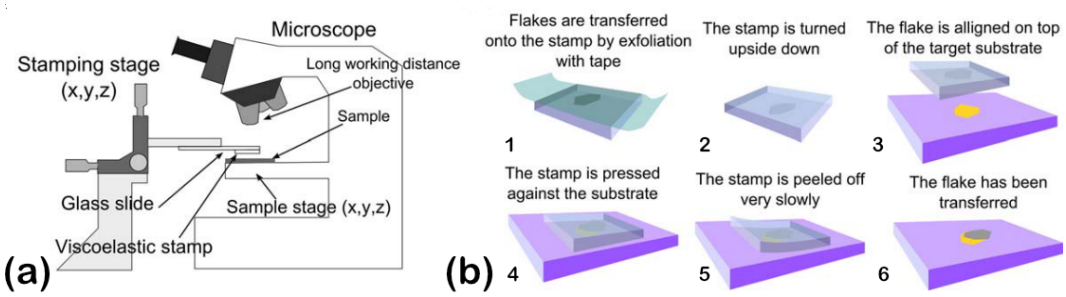

Figure 3.17: Transfer of flake onto a target substrate with the dry transfer technique. Taken from ref. [68].

If the flakes need to be deposited onto a specific structure or substrate the dry transfer technique is used. The dry transfer technique is useful as it doesn't leave behind residues and is easy to perform. For the dry transfer technique a stamping stage and a microscope with a long working distance is needed. The stamping stage has a glass slide onto which a viscoelastic stamp is adhered to. The flakes are transfered onto the transparent viscoelastic stamp and turned upside down to face the substrate. Because the stamp is transparent, focus can be changed between the substrate and the flake. The sample is then slowly aligned on the substrate and brought into contact. The stamp is slowly peeled off the substrate, leaving the flake. This works because the stamp is viscoelastic and will slowly flow over long timescales [68].

3.4.3 Identification of monolayers

To identify monolayers optical contrast in an optical microscope can be used as an indicative method. Absorption of light depends on the optical path taken, which is affected by the thickness of a flake [69]. In figure 3.18a) an image of a monolayer WSe_2 flake taken with an optical microscope is seen. By measuring samples of a known flake thickness, the optical contrast of the mono- and bilayer flakes on a substrate can be known. Commonly a Si wafer with a 285 nm thick SiO_2 layer on top is used as a substrate for the flakes. This SiO_2 layer thickness is used as it is known to give a high optical contrast for monolayer flakes. After a flake of desired thickness has been identified Raman spectroscopy and atomic force microscopy (AFM) is used to verify the thickness.

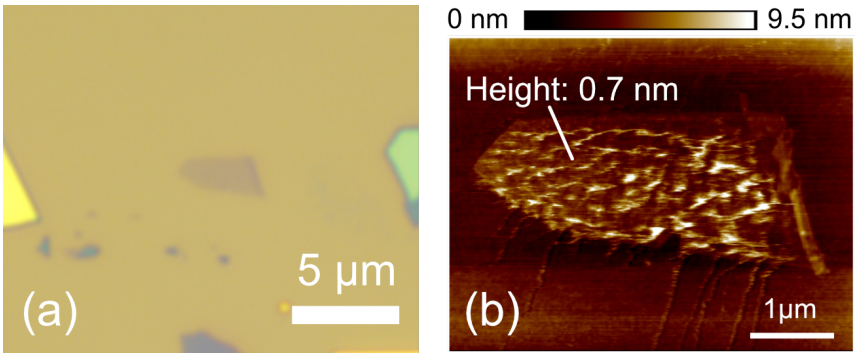

Figure 3.18: **a)** Image of monolayer WSe_2 flake visible by optical contrast. **b)** AFM image of monolayer with thickness of flake marked out.

AFM uses a cantilever and scans it along the surface of the material. As the cantilever follows the surface of the sample it will adjust and bend. The position and angle of the tip will be sensed by reflecting a light on the back of the lever. This will give the topography of the sample which is useful to see changes in thickness, but can be insufficient to determine if a flake is a monolayer or not. In figure 3.18b) the topography of a monolayer flake is shown. On the image some noise can be seen, which cause spikes in the measurement.

Raman spectroscopy works by analysing Raman scattering, which happens when light is inelastically scattered by vibrational modes in a molecule. The spectrum of the scattered light is measured and the shift from the incident light is recorded. The vibrational modes of TMD materials change with the number of layers as seen in figure 3.19. The spectrum can then be used to characterise the thickness of a flake. A distinct peak at 250 cm^{-1} is visible for mono- and bilayer WSe_2 with a small signature peak at 309 cm^{-1} visible only in bilayer form [30] but missing for monolayers.

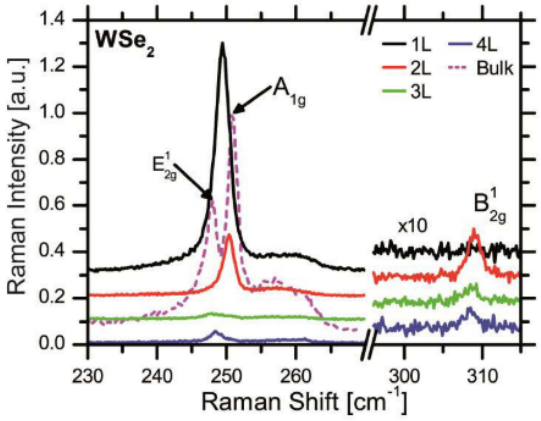

Figure 3.19: Raman shift of bulk and few-layer WSe_2 with the peaks used to identify mono- and bilayer flakes marked out. Taken from ref. [30].

To preserve the sample and minimise exposure to atmosphere, Raman spectroscopy and AFM is not done until after the PL measurements are finished. Beside these measurements the PL spectrum can also be used to identify the thickness emission

as the neutral exciton is only visible in monolayer flakes, seen previously in figure 2.11.

4

Results

To investigate quantum emission in 2D materials two different WSe_2 samples were investigated. The first sample was a 5 nm thick fewlayer (FL) flake, which was intended to test the set-up but showed interesting PL emission and was investigated further. The second sample was a monolayer flake, which was placed on a nanopillar. Large area PL was observed, as well as localised emitters on the pillar apex. The PL characteristics was analysed and compared to work reported in the literature.

During the experimental part of this work, the set-up was continuously upgraded and optimised. Therefore, some measurements were limited by the available functions of the set-up at that time. The results were used for important feedback on what parts and functions needed to be changed.

The experiments were selected to identify characteristics of SPEs in TMDs such as: narrow linewidth, saturation behaviour and nanosecond lifetime. Additional measurements were performed to characterise the nature of the emission such as polarisation and temperature dependence. To fully confirm the quantum nature the $g^{(2)}$ function would need to be measured. During this work that was not possible however.

4.1 Strained WSe_2 fewlayer

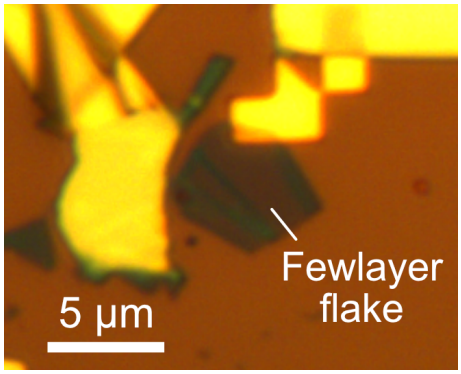

Figure 4.1: Image of the folded flake taken with an optical microscope.

The first sample was made to test the set-up for PL measurements and can be seen in figure 4.1. WSe_2 flakes were fabricated with the scotch-tape method and transferred onto a Si/SiO_2 chip with prefabricated coordination markers. From the optical contrast it was first characterised as a monolayer flake and was therefore

selected for measurements. From the microscope image of the sample darker lines are seen which were attributed to a folded structure in the flake or thicker regions left after the exfoliation. A folded structure would create strain which would help in the generation of quantum emitters.

When performing an AFM measurements of the sample it was found that the flake was in fact a FL flake with a thickness of around 5 nm seen in figure 4.2a). A rough estimate of the number of layers can be given from the thickness, which yields 7 layers, with 0.7 nm per layer [70].

Additionally, the flake had been placed unintentionally on top of a nanopillar structure part of the coordination markers, seen in figure 4.2b). The pillar had a height of around 73 nm and a FWHM diameter of 650 nm, seen in figure 4.2c). An uneven flake thickness can be discerned from the cross-section, which could indicate a folded structure, although SEM would be required to confirm this.

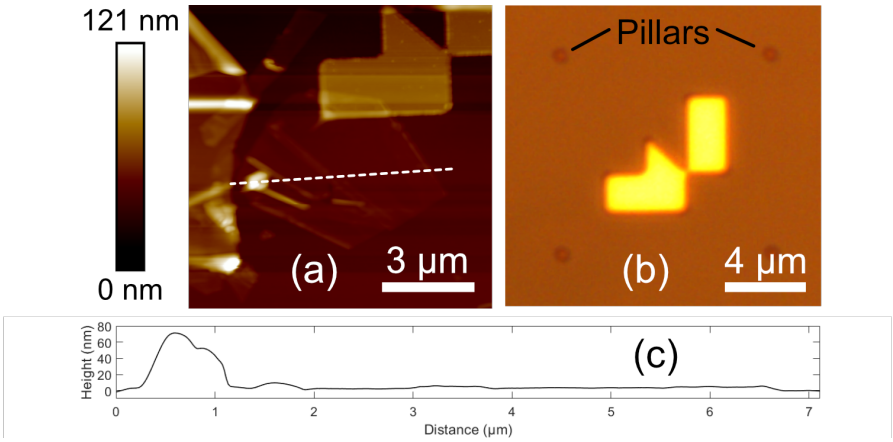

Figure 4.2: **a)** Structure of the folded FL measured with AFM. Horizontal lines are visible in the image which are artefacts of the AFM raster scan and can be ignored. Marked with a dotted white line is the cross section which is shown in **c)**. **b)** An optical microscopy image of another coordination markers where pillars can be seen in the corners. **c)** Height distribution along the length of the flake. A peak of around 73 nm can be seen where the flake is placed on top of the coordination marker nanopillar.

Raman spectroscopy was unfortunately not possible, as there was technical problems with the machine during the span of this work. However, Raman spectroscopy is only useful to determine if a flake is a monolayer or bilayer and can not be used to determine the thickness of FL flakes.

4.1.1 Localised emitters

The sample was placed in the cryostat and cooled down for low temperature measurements. A PL map was taken of the sample, which showed localised emission centers at the location of the nanopillar. Other emitters were also found on the FL flake as well as on sub-micron sized flakes on the Si/SiO_2 substrate. In figure 4.3a) the emitters are seen after above band gap excitation with the 470 nm LED. With

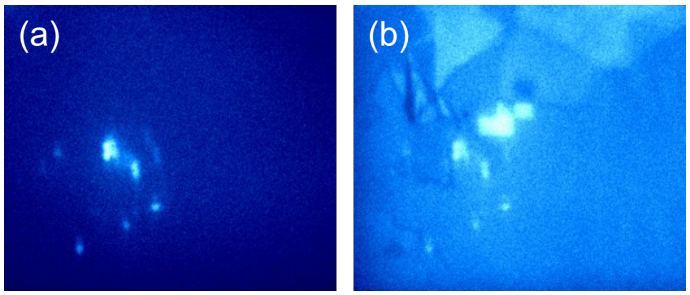

Figure 4.3: PL map and sample image recorded with the entire spectral range above 550 nm. **a)** PL map generated by large area excitation with a 470 nm LED. **b)** An image of the sample and localised emitters taken with the CCD. Acquired by exciting with the 470 nm LED and illuminating with the 730 nm LED simultaneously.

both the 470 nm LED and the 730 nm LED on at the same time, the position of the emitters on the flake can be seen in figure 4.3b).

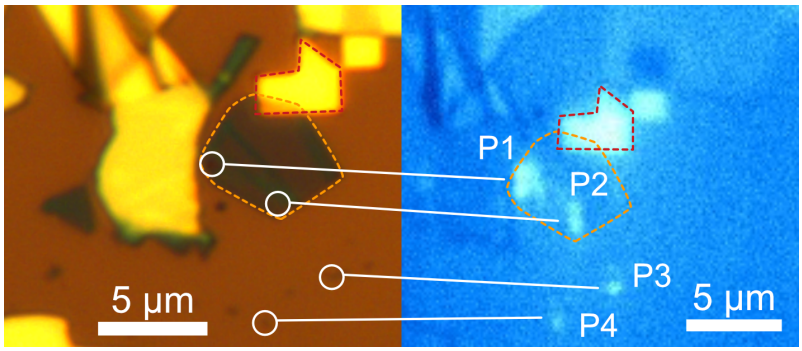

Figure 4.4: Location of emitters in the flake sample. Two emitters are found on the larger FL flakes and the other two are found on individual sub-micron sized flakes. Image on the right side is recorded with the entire spectral range above 550 nm.

In figure 4.4 the location of the emitters on the FL flake are marked out. At $P1$, which is the location of the nanopillar, there appears to be multiple emitters overlapping. Characterisation of these emitters could therefore prove difficult, as spatial separation is required in order to analyse individual emitters. A PL spectrum was taken at the location of the four emitters which is shown in figure 4.5. In the measurements a 1200 l/mm grating was used which gives a spectral resolution around 42.6 µeV at 1.55 eV.

The PL spectrum of the localised emitters was taken by excitation with the 470 nm LED and using fiber coupling to spatially filter the signal. Due to the weak emission intensity, a long exposure time of 10 s had to be used. The measured PL spectra are shown in figure 4.5.

The localised emitters on the flake show the strongest PL intensity, seen in figure 4.5a) and b). At the locations a band with narrow emission peaks is found around 1.55 eV ($\approx$ 800 nm). From the PL spectrum at P1, sharp emission peaks with

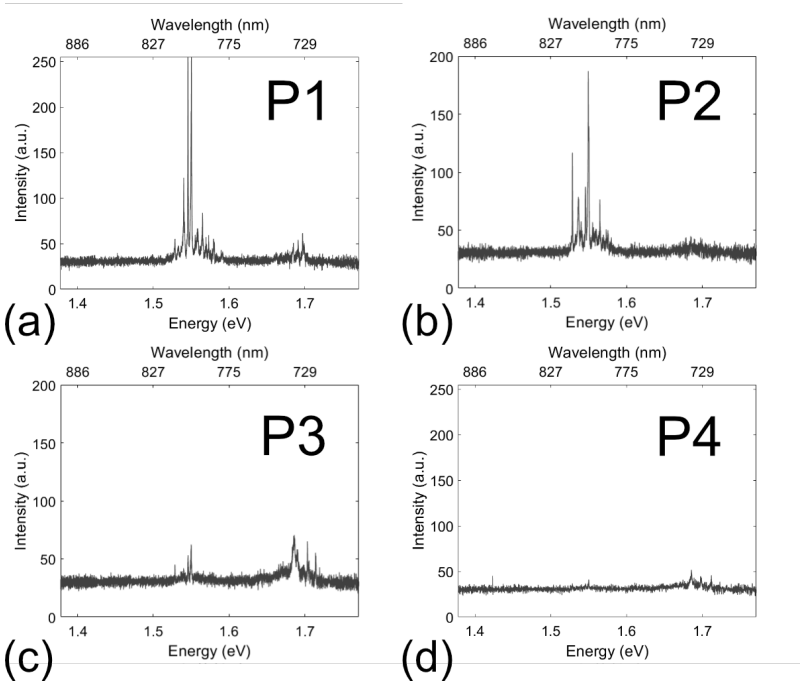

Figure 4.5: PL spectrum taken at the location of each of the marked emitters in figure 4.4.

linewidths around (450-850) µeV are measured. From other work we know that linewidths smaller than 2.3 meV is a promising indication of quantum emission [19], although linewidths around (100-200) µeV are more commonly reported [21, 23, 35]. Due to the long exposure time, inhomogenous broadening is expected from spectral jitter and the actual linewidths are likely smaller than those measured. More details on this is shown in section 4.1.4.

Currently there are not many studies on defect emission from FL WSe_2 and a comparison is difficult to make. In the work done by Kumar, S. et al. [22], strained bilayer WSe_2 flakes show emission peaks at 1.56 eV which appear to be brightening of the dark indirect exciton by strain. This is possibly the case for the observed defect emission in FL flakes as well.

From the PL spectrum of the sub-micron flakes in figure 4.5c) and b), the emission is very weak leading to a noisy measurement. Therefore a linewidth of any individual peak is difficult to determine. While very weak emission is observed at 1.55 eV, most emission is found around 1.7 eV which fit the emission range of the defect band in monolayer flakes. This band is also present in a) and b) and is very weak in all cases (< 50 counts).

The localised emitters on the FL flake showed the strongest emission and were investigated further. However, when repeating PL measurements, the same PL spectrum could not always be replicated. The reason for this is thought to be the low stability of the emitters and/or the density of emitters at one location, which made it difficult to collect from the exact same place. As a result, the emission spectra from following measurements differ and are sometimes taken at different locations on the FL flake.

4.1.2 Temperature dependence

In figure 4.6a) the temperature dependence in the range of 4.6 K to 80 K is shown. Starting with 30 K the localised emitters disappear after which there is almost no emission present anymore. This is an expected behaviour for defect emission when the thermal energy k_BT increases. When the thermal energy becomes higher than the ionisation energy of the defect state, trapping will be less efficient and defect emission will decrease [71].

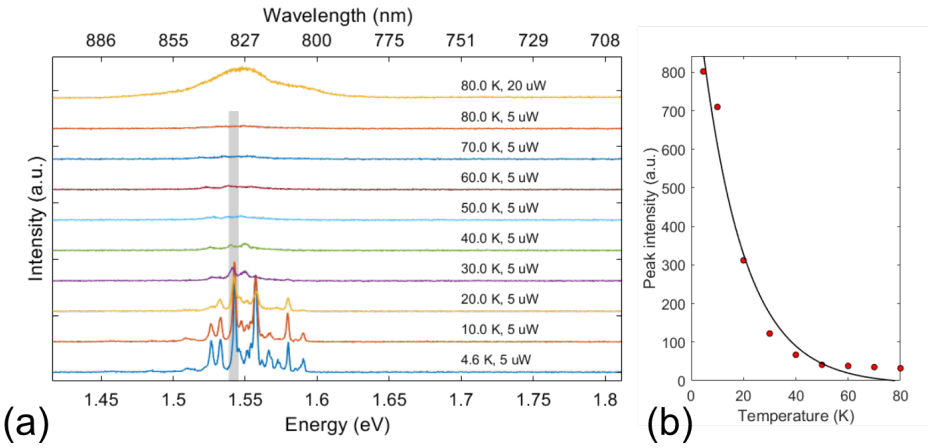

Figure 4.6: a) Temperature dependence of folded FL of WSe_2. Taken with pulsed laser at 5 and 20 µW. **b)** Maximum intensity of the emission peak at 1.542 eV depending on temperature shown in logarithmic scale. Fitted with the function $I(T) = I_0 \cdot e^{(-k_BT/E_a)} + \mathrm{C}$, yielding $E_a = 1.35^{+0.47}_{-0.27}$ meV, with a 95 % confidence interval.

The ionisation energy E_a of the trapped states can be modeled by the equation $I(T) = I_0 \cdot exp(-k_BT/E_a)$ and fitted to the measurements. In figure 4.6b) The maximum intensity of the emission peak at 1.542 eV is shown for changing temperature and an excitation power of 5 µW. For this equation the intensity of the peak is assumed to belong to only one defect state. From the fit an ionisation energy of 1.35 meV is found. The peak at 1.555 eV was also measured which yielded an activation energy of $0.91^{+0.21}_{-0.15}$ meV, with a 95 % confidence interval (not shown). For WSe_2 the defect trapping is around 300 µeV in monolayer flakes [47] and 515 µeV in FL flakes [65].

Although the exponential fit has a rather large error, even the smallest value for E_a within the 95 % confidence range is double that reported for FL flakes. The reason for these deep traps observed are not known, but indicate that the nature of the traps are different from available references.

By increasing the excitation power, a broad PL emission band is seen which is shown for 80 K in figure 4.6a). This broad band appears to consist of two broad peaks that overlap. One possibility is that one belongs to the defect band, while the other belongs to the indirect exciton appearing at higher pump power, discussed more in section 4.1.3.

If the two emission peaks at high temperature belong to the defect band and the indirect exciton, a detuning energy of the defect emission can be extracted around 37.5 meV. Such a detuning energy is slightly smaller than those reported for monolayer flakes (40-200 meV) [19]. However, a second recombination channel is possible, where the emission stems from trapping of the direct exciton in a deep confinement potential. Although, due to the spectral density of defect emission at 1.55 eV and absence of defect emission in between, this is not believed to be the case.

Interestingly, the emission energy of the indirect exciton observed here agrees with that of bilayer WSe_2 flakes reported by A. Arora et al. [70]. The group also investigated FL flake emission, which found emission energies for the indirect exciton in the range (1.25-1.36) eV, which is outside the range of our findings. Further experiments such as power dependent measurements at room temperature need to be performed to identify the origin of the double peaks at higher temperature.

4.1.3 Power dependence

The PL spectrum was then measured at different power densities and individual emission peaks were analysed, showed in figure 4.7. In order to determine the power density the optical power was measured in front of the cryostat with a power meter and then divided by the FWHM area of the blue laser at 21.2 µm^2. The FWHM area is calculated from the diameter size measured and fitted to a gaussian shown in figure 3.6 in section 3.1.

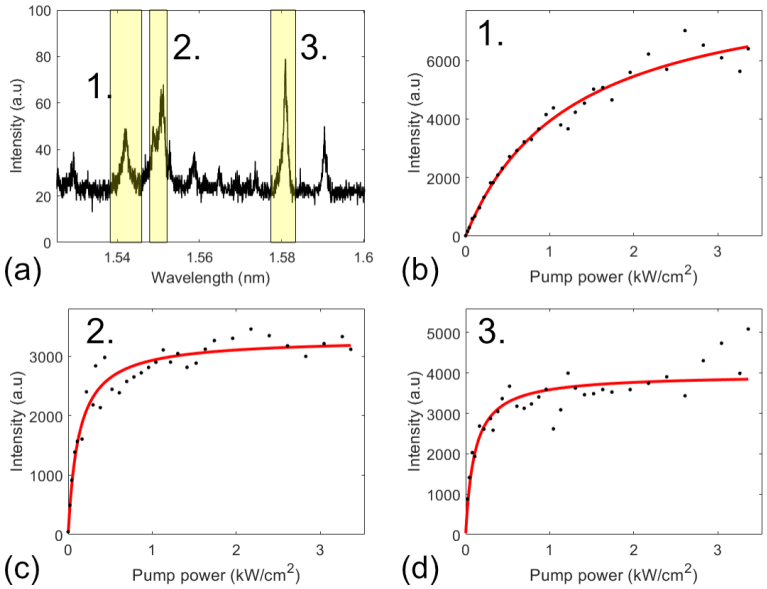

Figure 4.7: Power dependence of different emission peaks from the localised emitter on a nanopillar. **a)** A PL spectrum of the emitter with 88 µW excitation power at 4.6 K. Integrated regions used for saturation fitting are highlighted in yellow. **b-d)** Integrated emission intensity over an emission peak plotted against excitation power density. Shown in solid red is the data fitted to equation $I(P) = I_{sat} \cdot P/(P + P_{sat})$. The saturation power density P_{sat} is shown in table 4.1.

The power dependence varies between each emission peak with narrow linewidth, but all peaks observed show saturation behaviour. Such behaviour is expected for defect emitters, which can act as two-level systems [21]. The saturation power density P_{sat} for the emission peaks is determined by fitting the data to the equation $I_{sat} = P \cdot /(P + P_{sat})$ and is shown in table 4.1.

Figure number	1	2	3
Spectral range (eV)	1.538-1.546	1.548-1.552	1.577-1.584
P_{sat} ($\mathrm{W\,cm^{-2}}$)	1324	115	137

Table 4.1: Saturation power densities for emission peaks at different wavelengths shown in figure 4.7a)

In the paper from Tonndorf et al. 2015 a saturation power density of $3\,\mathrm{kW\,cm^{-2}}$ is measured for monolayer WSe_2 [19]. For two level systems the saturation power density is determined by the lifetime of the defect state. Longer lifetimes will generate less emission and saturation is reached quickly. From the saturation behaviour observed, the emitters are therefore expected to have longer lifetimes than Tonndorf et al (1.8-6.5 ns).

The delocalised exciton emission intensity follows a linear power dependence while defect emission follows a sub-linear dependence [55, 71]. To be able to measure delocalised emission a higher excitation power is therefore needed. Subsequently, the PL spectrum at low excitation power will consist primarily of defect emission.

4.1.4 Spectral stability

The stability of the emitters is very important for the application of SPEs. In order to measure this stability the PL spectrum is taken for 12.5 min with 1.5 s exposure time for each measurement. The PL spectrum over the time period is seen in figure 4.8 with an excitation power of $47.2\,\mathrm{W\,cm^{-2}}$ and $94.4\,\mathrm{W\,cm^{-2}}$. The emission peaks

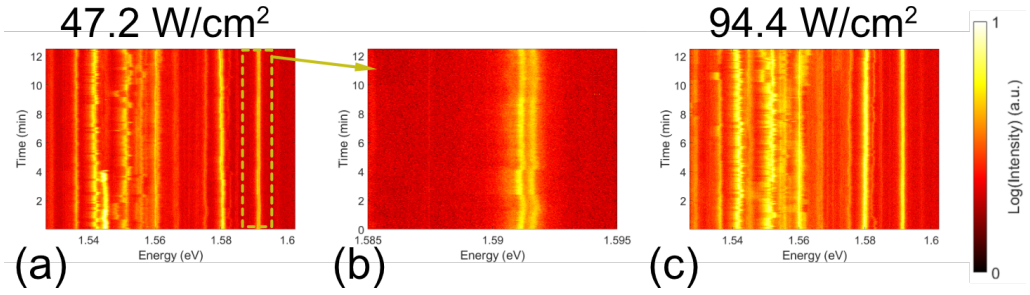

Figure 4.8: Spectral wandering taken over 12.5 min with PL spectrum taken every 1.5 second. **a)** Excitation power density at $43.5\,\mathrm{W\,cm^{-2}}$ **b)** Spectral wandering at 1.59 eV shown with high resolution. **c)** Excitation power density at $87\,\mathrm{W\,cm^{-2}}$.

are relatively stable over time and have a spectral wandering smaller than 2 meV. This is rather low for non-resonant PL emission and similar to the spectral wandering of quantum emitters in monolayer WSe_2 (2.5 meV) [19]. Resonant excitation is

expected to result in lower spectral wandering as there are no additional charges generated from pumping to CB [19].

However, the peak at 1.59 eV, shown in figure 4.8c) shows excellent stability with a spectral wandering below 180 µeV. The peak consists of a doublet separated by 500 µeV. The two peaks show synchronised wandering behaviour which has been observed in prior work [21, 47, 62] and indicates that they originate from the same localised state. The splitting can be associated with electron-hole exchange interactions which could be explored with magneto-optical spectroscopy [47].

In figure 4.8a) the emission peak at 1.545 eV disappears four minutes into the measurement. At a later measurement not shown, the peak returned again. This effect is called blinking behaviour which could be caused by charge fluctuations in the environment of the localised emitter [21] and is detrimental for quantum emitters.

4.1.5 Emission polarisation

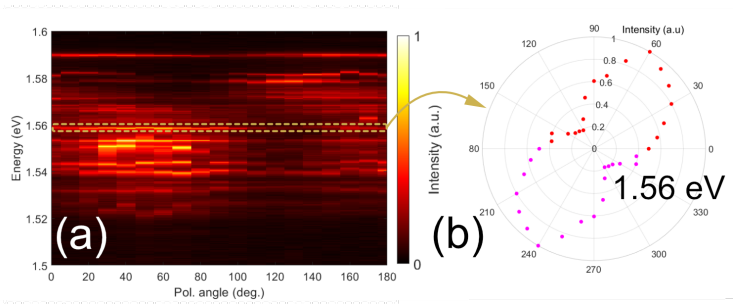

Figure 4.9: a) Polarisation dependent PL spectrum with polarisation angle from 0 - 180°. **b)** Polar representation of the maximal intensity for the emission peak at 1.578. Data was collected for 180° but is assumed to be symmetric. The data is therefore repeated, shown in pink.

Polarisation dependent PL spectrum was measured over 180°, shown in figure 4.9. By measuring the emission peak at 1.56 eV, a linear polarisation behaviour was found with 90° between the maximum and minimum intensity, seen in figure 4.9b). This is indicative of a dipole emitter, found in localised emitters in strained WSe_2 [19]. However, another paper done by W. Wu et al. [65] investigated FL WSe_2 flakes strained by a ultrasharp SiO_2 tip and no polarisation dependence was found. The emission nature for the FL tested in this work appears to have closer similarities to localised emitters in monolayer flakes. The different emission peaks show different polarisation angles, which might be caused by anisotropic strain in our FL [19].

Another polarisation dependence that must be taken into account is that of the 1200 l/mm grating. In the wavelength range measured in figure 4.9 the efficiency is 71 % for s-polarised light and 44 % for p-polarised light. Therefore p-polarised light intensity will be around 62 % of s-polarised light. We measure a minimum intensity of less than 25 % of maximum light intensity and can therefore attribute the polarisation dependence to the emitters with good confidence. To remove the polarisation dependence of the grating, PL emission could be passed through a

depolarise after the linear polariser. Then, the polarisation will be randomised, which will remove any polarisation dependence in the grating.

4.1.6 Time resolved photoluminescence

TRLP measurements were taken to investigate the lifetime and $g^{(2)}$ of the localised emitters of the folded FL flake. In order to investigate the emission peaks individually, the emission light should ideally be spectrally filtered. At the time of the lifetime measurement, the monochromator set-up was not ready and the measurements had to be taken for the entire PL spectrum. The result is therefore an average lifetime measurement of the total PL emission.

Lifetime

The lifetime was measured with the 485 nm laser at 30 MHz pulse mode, which can be seen for 90.5 W cm^{-2} excitation power in figure 4.10a). The optical power density ranged from (1.7 - 90.5) W cm^{-2} and some emitters can be expected to start saturating at high pump power. At low pump power the defect emission is expected to dominate the PL spectrum while at higher pump power more contribution is expected from the indirect exciton.

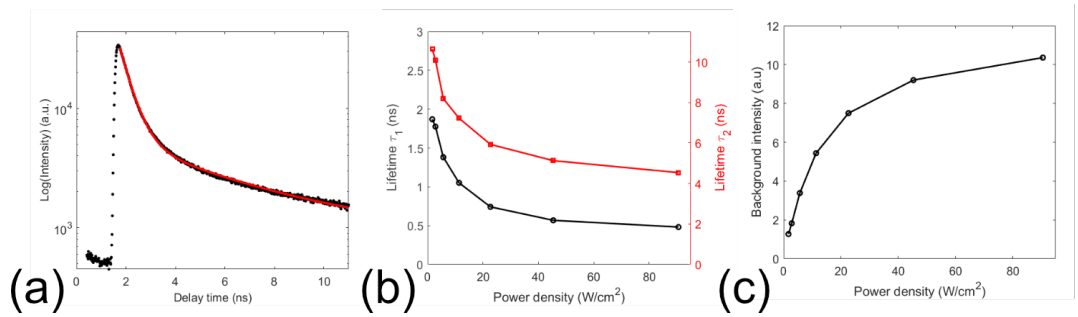

Figure 4.10: a) Lifetime of the PL emission at 90.5 W cm^{-2} shown in logarithmic scale. Shown in red is a fit of the lifetime measurement to a biexponential with a background constant. **b)** Power dependence of the two lifetimes calculated. Note the different time scales on the y axes. **c)** Power dependence of the background intensity.

When excited deep in the CB the electrons must first relax down to the CBM. This intraband relaxation process is a fast process in the range of around 20 ps for bulk WSe_2 and less than 500 fs for monolayer WSe_2 [56]. This is faster than the timing resolution of the set-up that is around 250 ps and is therefore not detectable. The decay times measured should therefore describe recombination processes after the carriers have relaxed to the CBM.

The lifetime measurements acquired could only be fitted by a double exponential decay with a background constant expressed as

$$I(t) = C_1 \cdot e^{-\frac{t}{\tau_1}} + C_2 \cdot e^{-\frac{t}{\tau_2}} + I_{bg} \tag{4.1}$$

where I is intenisty, t is time, C_i are constants, τ_i are lifetimes and I_{bg} is background intensity. As spectral filtering was not possible for the measurements, multiple emitters are measured at the same time. The two lifetimes determined are therefore attributed to different emitters.

The two lifetimes depend on excitation power which can be seen in figure 4.10b). This behaviour is currently attributed to exciton-exciton interactions, which increases with higher exciton occupation [72]. Additionally, due to the localised heating of the laser, phonon scattering increases which quenches the emission [73].

The first lifetime is around (0.48 - 1.87) ns and the second is around (4.54 - 10.63) ns, which is in the range reported in literature. The lifetimes reported for monolayer WSe_2 flakes are usually in the range (0.5 - 6.5) ns [19, 21–23, 35, 47], although longer lifetimes are not uncommon [65, 74].

However, when fitting the lifetime measurements the background intensity was found to depend on the excitation power, shown in figure 4.10c). As such, the background is not only caused by ambient light or dark counts, which would not depend on excitation power. Therefore, the light must come from emission from the sample. Additionally, since the background is virtually constant over the duration of the measurement, the emission must come from a source with lifetime at least longer than the laser pulse period (33 ns). From calculation performed on lifetime in MoS_2, dark states in bilayer and bulk flakes could show lifetimes in the range of a few µs [57]. As group-VI TMDs have similar excitonic physics, these calculations are taken as an indication that similar long lived dark states are present in WSe_2 as well. Therefore, the background intensity is attributed to the radiative recombination from such dark states, such as the indirect exciton.

Time correlation

Due to the lack of spectral filtering and the low intensity of the emitters a $g^{(2)}$ function measurement could not be performed. However, if the source was a SPE a small dip where $g^{(2)}(0) < 1$ could be expected given a long enough measuring time. The previous measurements had shown indicators of quantum emission, such as narrow linewidth, saturation behaviour and nanosecond lifetimes. However, due to the low signal to noise ratio no proper $g^{(2)}(\tau)$ was measured.

The low efficiency is largely due to the SPAPDs we use which are optimised for timing resolution but have low quantum efficiency (12-20 %) in the spectral range (700-800) nm. To measure the $g^{(2)}$ function a source with higher emission intensity and/or different SPAPDs would be required.

4.1.7 Cyclic stability

After cycling from 4.6 K to room temperature and back the location of the emitters had changed, seen in figure 4.11. There were still emitters present at strained regions of the FL flake, but the location had changed compared to those in figure 4.11c). Additionally, before temperature cycling there appeared to be multiple localised emitters in clusters. Whereas, after temperature cycling there seem to be fewer emitters.

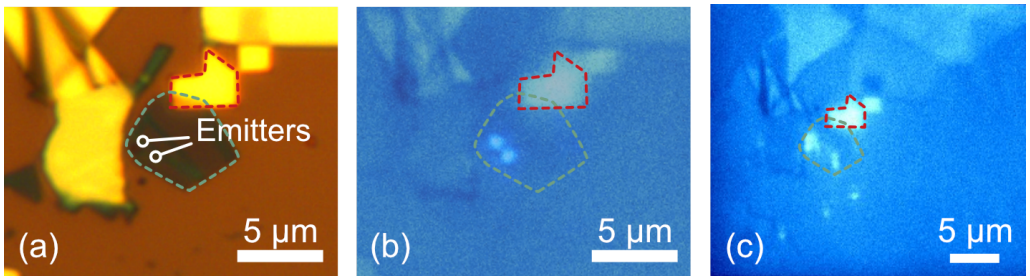

Figure 4.11: Location of emitters on folded FL after temperature cycling from 4.6 K → 292 K → 4.6 K. **a)** Image of the sample with location of the emitters marked out. **b)** Location of emitters after temperature cycling. Image generated by superimposing image illuminated with a 730 nm LED and PL map excited with a 470 nm LED. **c)** Location of emitters before temperature cycling. Image generated by illuminating with 730 nm LED and exciting with 470 nm LED simultaneously.

When returning to room temperature the sample is heated and the temperature changes rapidly. Therefore the sample is thought to experience annealing during the heating process which removed strain or defects responsible for localised emitters.

4.2 Monolayer on nanopillar sample

To measure the $g^{(2)}$ function a more stable sample with strong localised emission was needed. Therefore, WSe_2 flakes were exfoliated and a monolayer identified with optical contrast. The flake was then transferred onto a 200 nm tall nanopillar with a width of 100 nm, seen in figure 4.12a). A PL map is taken by exciting with the 470 nm LED which reveal a localised emission from the monolayer at the location of the nanopillar, shown in figure 4.12b). Moreover, strong emission is measured from the entire flake, which is expected from a monolayer flake due to its direct band gap.

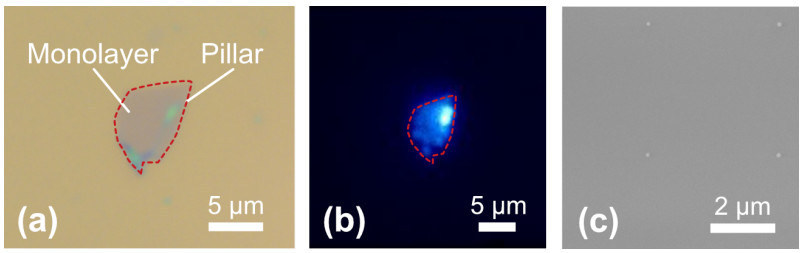

Figure 4.12: **a)** Microscope objective image of a WSe_2 monolayer flake placed on top of a pillar. **b)** PL map of the monolayer on top of the pillar. Strong localised PL emission can be seen from the pillar location. **c)** SEM image of the nanopillars that the flake was placed on.

The nanopillars were fabricated by spincoating a wafer with a UVN resist, which created a 200 nm thick film. The resist was then patterned with electron beam

lithography (EBL) and chemically etched to create circular pillars with varying diameters, seen in figure 4.12c).

4.2.1 Localised emitter

The PL spectrum of the localised emitter was measured, shown in figure 4.13. Once again sharp emission lines with a linewidth of 220 µeV were found at 1.688 eV, detuned from the neutral exciton X^0 by around 72 meV. This is in line with reported values for quantum emitters in monolayer WSe_2 flakes, where a detuning of (40 - 200) meV was measured [19].

In figure 4.13a) the neutral exciton emission peak can be seen and becomes distinct at higher optical powers(not shown), further confirming that the sample is a monolayer flake. For many samples an emission peak for the trion is also visible at 1.71 eV, which arises from inadvertent doping of the flake by defects such as atomic vacancies [61]. In our sample the trion is however absent, which suggests that the flake is approximately intrinsically doped [75], i.e. that the Fermi level is located in the middle of the band gap. At low excitation power the defect emission splits into separate peaks, seen in figure 4.13b). The marked emission peak at 1.688 eV exhibits the strongest PL intensity and is spectrally filtered for lifetime measurements.

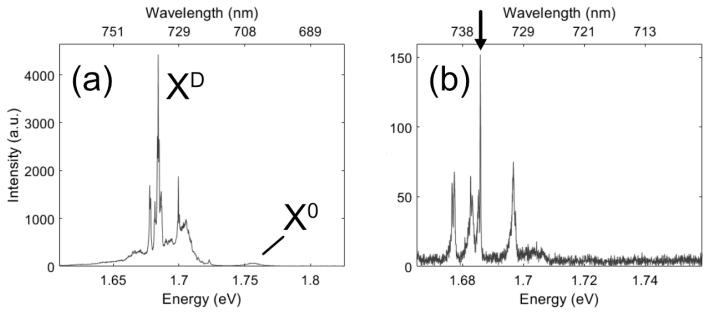

Figure 4.13: **a)** PL spectrum from monolayer WSe_2 flake placed on top of a nanopillar. **b)** PL taken with low excitation power with the peak used for lifetime measurements marked out.

4.2.2 Lifetime

The intensity of the PL emission from the sample was stronger than that of the FL flake and time dependent measurements were taken. Spectral filtering was now available and used to filter the peak at 1.688 eV, marked in figure 4.13b). The sample was excited with a pulsed laser with 80 MHz repetition rate and life time was measured, seen in figure 4.14.Due to the spectral filtering the signal was decreased significantly and a measurement time of 40 minutes was used to get the lifetime. Additionally the signal-to-noise ratio was small, which resulted in a large data point spread.

For this measurement a single exponential function with a background constant was

used to fit the data, expressed as

$$I(t) = C \cdot e^{-\frac{t}{\tau}} + I_{bg} \tag{4.2}$$

where I is intensity, t is time, C is a constant, τ is lifetime and I_{bg} is background intensity. From the fit a lifetime at 1.97 ns was extracted. This is well within the expected lifetimes of quantum emission in other monolayer samples.

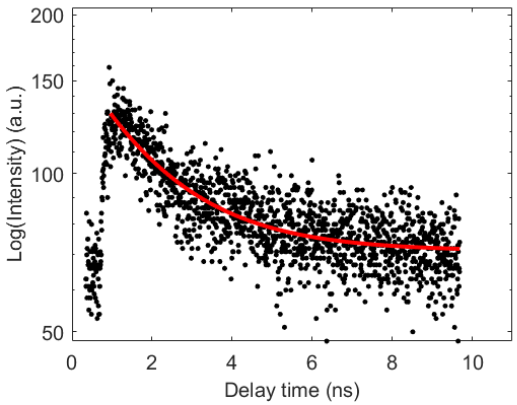

Figure 4.14: Lifetime of the localised emitter on top of strained monolayer flake. Measurement is taken for spectrally filtered with center at 1.688 eV with a FWHM of 0.5 meV. A single exponential fit with a background constant yielded a lifetime at 1.97 ns, with 95 % confidence interval at (1.88 - 2.07) ns.

The PL intensity was higher for the monolayer WSe_2, and an attempt was made to measure the $g^{(2)}$ function. The measurement could not generate useful data however, which made us aware of a problem with one of the SPAPDs. One of the SPAPD generated afterpulses approximately 12 ns following a photon detection event. Therefore, periodic interference effects were present and a $g^{(2)}$ measurement could not be possible using the available SPAPDs. Additionally. further testing showed that the efficiency of the SPAPDs was too low and the signal-to-noise ratio made $g^{(2)}(\tau)$ measurements impossible with the PL emission strength of the localised emitters measured here.

4.3 Summary

During the course of this work, the $g^{(2)}$ function could not be measured and the quantum nature remains unconfirmed. Going forward, the set-up needs to be optimised before measuring the $g^{(2)}(\tau)$ function.

However, the results showed promising characteristics of quantum emission in monolayer and FL flakes. Both show sharp emission lines 220 µeV - 2.5 meV and lifetimes in the nanosecond range (0.48 - 10.63) ns. Addionally, power dependence and temperature dependence measurements for the FL flake showed that the emission was defect based with saturation power densities around (115-1324) W cm^{-2}.

5

Conclusion & outlook

In this work, PL emission was investigated in WSe_2 flakes. To conduct these measurements a complete optical set-up was built and optimised. Using measurements such as micro-photoluminescence microscopy, TRPL and time-correlation measurement the nature of localised emission in WSe_2 flakes was measured.

By placing mono- and fewlayer WSe_2 onto nanopillar structures, localised emitters were successfully created on the strained regions. The PL spectrum from these localised emitters show characteristics of quantum emitters from other works, such as sharp emission lines (linewidth < 2.3 meV), saturation behaviour (100-1270 $\mathrm{W\,cm^{-2}}$), strong temperature dependence (1.3 meV ionisation energy) and lifetime in the range of a few ns (0.48-10.6 ns). When considered as a whole, these measurements strongly indicate that the localised emitters are single photon sources. However, to confirm this claim the $g^{(2)}$ function needs to be measured, which was not possible in the span of this work.

To measure the $g^{(2)}$ function, which is indispensable to analyse SPEs, samples with stronger PL intensity are required. Additionally, the collection efficiency of the set-up needs to be optimised for low transmission loss and high detection efficiency in the expected spectral range of the emission. This is an important point when constructing an optical set-up for quantum optics measurement and extra attention must be paid.

The localised emitters on the fewlayer flake showed little spectral wandering but suffered from blinking and cyclic instability. The reason for this is still not clear, but is attributed to thermal annealing of the flake. The intensity of these emitters was also rather low which require longer measuring times and made time-correlated measurements impossible. As fewlayer flakes show little advantages over localised emitters in monolayer flakes, we recommend that monolayers are used for PL characterisation testing.

Going forwards, the efficiency of the set-up will be improved to measure the $g^{(2)}$ function and confirm quantum light emission in the samples.

With a fully functioning set-up available new projects can be started. Two main projects are now being considered: The first is to place SPEs in monolayer flakes into optical cavities, thus enhancing their emission intensity due to the Purcell effect. The second interesting field is single photon emission in heterobilayer moiré structures. This is an emerging topic, where the twist angle between two monolayer flakes is used to engineer the excitonic band structure.

Bibliography

[1] Scott E. Thompson and Srivatsan Parthasarathy. Moore's law: the future of Si microelectronics. *Materials Today*, 9(6):20–25, jun 2006.

[2] Richard P. Feynman. Simulating physics with computers. *International Journal of Theoretical Physics*, 21(6-7):467–488, jun 1982.

[3] P.W. Shor. Algorithms for quantum computation: discrete logarithms and factoring. In *Proceedings 35th Annual Symposium on Foundations of Computer Science*, pages 124–134. Institute of Electrical and Electronics Engineers (IEEE), dec 2002.

[4] Charles H. Bennett. Quantum cryptography using any two nonorthogonal states. *Physical Review Letters*, 68(21):3121–3124, may 1992.

[5] Fulvio Flamini, Nicolò Spagnolo, and Fabio Sciarrino. Photonic quantum information processing: a review. *Reports on Progress in Physics*, 82(1):016001, nov 2019.

[6] M. D. Eisaman, J. Fan, A. Migdall, and S. V. Polyakov. Invited Review Article: Single-photon sources and detectors. *Review of Scientific Instruments*, 82(7):071101, jul 2011.

[7] CH Bennett and Gilles Brassard. Proceedings of the IEEE International Conference on Computers, Systems and Signal Processing, Bangalore, India. *IEEE, New York*, 175:8, 1984.

[8] E. Knill, R. Laflamme, and G. J. Milburn. A scheme for efficient quantum computation with linear optics. *Nature*, 409(6816):46–52, jan 2001.

[9] D. B. Higginbottom, L. Slodička, G. Araneda, L. Lachman, R. Filip, M. Hennrich, and R. Blatt. Pure single photons from a trapped atom source. *New Journal of Physics*, 18(9), 2016.

[10] Julia Benedikter, Hanno Kaupp, Thomas Hümmer, Yuejiang Liang, Alexander Bommer, Christoph Becher, Anke Krueger, Jason M. Smith, Theodor W. Hänsch, and David Hunger. Cavity-Enhanced Single-Photon Source Based on the Silicon-Vacancy Center in Diamond. *Physical Review Applied*, 7(2):024031, feb 2017.

[11] M. Benyoucef, S. M. Ulrich, P. Michler, J. Wiersig, F. Jahnke, and A. Forchel. Enhanced correlated photon pair emission from a pillar microcavity. *New Journal of Physics*, 6:1–12, 2004.

[12] Pascale Senellart, Glenn Solomon, and Andrew White. High-performance semiconductor quantum-dot single-photon sources, nov 2017.

[13] N. Somaschi, V. Giesz, L. De Santis, J. C. Loredo, M. P. Almeida, G. Hornecker, S. L. Portalupi, T. Grange, C. Antón, J. Demory, C. Gómez, I. Sagnes, N. D. Lanzillotti-Kimura, A. Lemaítre, A. Auffeves, A. G. White, L. Lanco, and P. Senellart. Near-optimal single-photon sources in the solid state. *Nature Photonics*, 10(5):340–345, may 2016.

[14] Lucas Schweickert, Klaus D. Jöns, Katharina D. Zeuner, Saimon Filipe Covre Da Silva, Huiying Huang, Thomas Lettner, Marcus Reindl, Julien Zichi, Rinaldo Trotta, Armando Rastelli, and Val Zwiller. On-demand generation of background-free single photons from a solid-state source. *Applied Physics Letters*, 112(9):093106, feb 2018.

[15] Xing Ding, Yu He, Z. C. Duan, Niels Gregersen, M. C. Chen, S. Unsleber, S. Maier, Christian Schneider, Martin Kamp, Sven Höfling, Chao Yang Lu, and Jian Wei Pan. On-Demand Single Photons with High Extraction Efficiency and Near-Unity Indistinguishability from a Resonantly Driven Quantum Dot in a Micropillar. *Physical Review Letters*, 116(2):020401, jan 2016.

[16] Peter Lodahl. Quantum-dot based photonic quantum networks. *Quantum Science and Technology*, 3(1), 2018.

[17] Jeremy L. O'Brien, Akira Furusawa, and Jelena Vučković. Photonic quantum technologies, dec 2009.

[18] Carlos Errando-Herranz, Eva Schöll, Raphaël Picard, Micaela Laini, Samuel Gyger, Ali W. Elshaari, Art Branny, Ulrika Wennberg, Sebastien Barbat, Thibaut Renaud, Mauro Brotons-Gisbert, Cristian Bonato, Brian D. Gerardot, Val Zwiller, and Klaus D. Jöns. Resonance fluorescence from waveguide-coupled strain-localized two-dimensional quantum emitters, feb 2020.

[19] Philipp Tonndorf, Robert Schmidt, Robert Schneider, Johannes Kern, Michele Buscema, Gary A. Steele, Andres Castellanos-Gomez, Herre S. J. van der Zant, Steffen Michaelis de Vasconcellos, and Rudolf Bratschitsch. Single-photon emission from localized excitons in an atomically thin semiconductor. *Optica*, 2(4):347, apr 2015.

[20] Yu Ming He, Genevieve Clark, John R. Schaibley, Yu He, Ming Cheng Chen, Yu Jia Wei, Xing Ding, Qiang Zhang, Wang Yao, Xiaodong Xu, Chao Yang Lu, and Jian Wei Pan. Single quantum emitters in monolayer semiconductors. *Nature Nanotechnology*, 10(6):497–502, jun 2015.

[21] Ajit Srivastava, Meinrad Sidler, Adrien V. Allain, Dominik S. Lembke, Andras Kis, and A. Imamoglu. Optically active quantum dots in monolayer WSe 2. *Nature Nanotechnology*, 10(6):491–496, jun 2015.

[22] S. Kumar, A. Kaczmarczyk, and B. D. Gerardot. Strain-Induced Spatial and Spectral Isolation of Quantum Emitters in Mono- and Bilayer WSe2. *Nano Letters*, 15(11):7567–7573, nov 2015.

[23] M. Koperski, K. Nogajewski, A. Arora, V. Cherkez, P. Mallet, J. Y. Veuillen, J. Marcus, P. Kossacki, and M. Potemski. Single photon emitters in exfoliated WSe2 structures. *Nature Nanotechnology*, 10(6):503–506, jun 2015.

[24] Toan Trong Tran, Kerem Bray, Michael J. Ford, Milos Toth, and Igor Aharonovich. Quantum emission from hexagonal boron nitride monolayers.

Nature Nanotechnology, 11(1):37–41, jan 2016.

[25] A. K. Geim and I. V. Grigorieva. Van der Waals heterostructures. *Nature*, 499(7459):419–425, jul 2013.

[26] K. S. Novoselov, A. K. Geim, S. V. Morozov, D. Jiang, Y. Zhang, S. V. Dubonos, I. V. Grigorieva, and A. A. Firsov. Electric field in atomically thin carbon films. *Science*, 306(5696):666–669, oct 2004.

[27] Jiadong Zhou, Junhao Lin, Xiangwei Huang, Yao Zhou, Yu Chen, Juan Xia, Hong Wang, Yu Xie, Huimei Yu, Jincheng Lei, Di Wu, Fucai Liu, Qundong Fu, Qingsheng Zeng, Chuang Han Hsu, Changli Yang, Li Lu, Ting Yu, Zexiang Shen, Hsin Lin, Boris I. Yakobson, Qian Liu, Kazu Suenaga, Guangtong Liu, and Zheng Liu. A library of atomically thin metal chalcogenides. *Nature*, 556(7701):355–359, apr 2018.

[28] F. Bonaccorso, Z. Sun, T. Hasan, and A. C. Ferrari. Graphene photonics and optoelectronics. *Nature Photonics*, 4(9):611–622, sep 2010.

[29] Gang Wang, Alexey Chernikov, Mikhail M. Glazov, Tony F. Heinz, Xavier Marie, Thierry Amand, and Bernhard Urbaszek. Colloquium: Excitons in atomically thin transition metal dichalcogenides. *Reviews of Modern Physics*, 90(2):021001, apr 2018.

[30] Philipp Tonndorf, Robert Schmidt, Philipp Böttger, Xiao Zhang, Janna Börner, Andreas Liebig, Manfred Albrecht, Christian Kloc, Ovidiu Gordan, Dietrich R T Zahn, Steffen Michaelis De Vasconcellos, and Rudolf Bratschitsch. Photoluminescence emission and Raman. *Optics Express, Vol. 21, Issue 4, pp. 4908-4916*, 21(4):4908–4916, feb 2013.

[31] Manish Chhowalla, Hyeon Suk Shin, Goki Eda, Lain Jong Li, Kian Ping Loh, and Hua Zhang. The chemistry of two-dimensional layered transition metal dichalcogenide nanosheets, apr 2013.

[32] Keliang He, Nardeep Kumar, Liang Zhao, Zefang Wang, Kin Fai Mak, Hui Zhao, and Jie Shan. Tightly bound excitons in monolayer WSe2. *Physical Review Letters*, 113(2), jul 2014.

[33] J. Klein, M. Lorke, M. Florian, F. Sigger, L. Sigl, S. Rey, J. Wierzbowski, J. Cerne, K. Müller, E. Mitterreiter, P. Zimmermann, T. Taniguchi, K. Watanabe, U. Wurstbauer, M. Kaniber, M. Knap, R. Schmidt, J. J. Finley, and A. W. Holleitner. Site-selectively generated photon emitters in monolayer MoS2 via local helium ion irradiation. *Nature Communications*, 10(1):1–8, dec 2019.

[34] B. Amin, T. P. Kaloni, and U. Schwingenschlögl. Strain engineering of WS2, WSe2, and WTe2. *RSC Advances*, 4(65):34561–34565, aug 2014.

[35] Artur Branny, Santosh Kumar, Raphaël Proux, and Brian D. Gerardot. Deterministic strain-induced arrays of quantum emitters in a two-dimensional semiconductor. *Nature Communications*, 8, may 2017.

[36] Carmen Palacios-Berraquero, Dhiren M. Kara, Alejandro R.P. Montblanch, Matteo Barbone, Pawel Latawiec, Duhee Yoon, Anna K. Ott, Marko Loncar, Andrea C. Ferrari, and Mete Atatüre. Large-scale quantum-emitter arrays in atomically thin semiconductors. *Nature Communications*, 8(1):1–6, may 2017.

[37] D.F. Walls and Gerard J. Milburn. *Quantum Optics*. Springer, Berlin, 2 edition, 2008.

[38] Christopher Gerry and Peter Knight. *Introductory Quantum Optics*. Cambridge University Press, oct 2004.

[39] Zhiliang Yuan, Beata E. Kardynal, R. Mark Stevenson, Andrew J. Shields, Charlene J. Lobo, Ken Cooper, Neil S. Beattie, Michael Pepper, and Michael Pepper. Electrically driven single-photon source. *Science*, 295(5552):102–105, jan 2002.

[40] Mark (Anthony Mark) Fox. *Quantum optics : an introduction*. Oxford University Press, 2006.

[41] Hartmut Haug and Stephan W. Koch. *Quantum theory of the optical and electronic properties of semiconductors, fifth edition*. World Scientific Publishing Co., 5 edition, jan 2009.

[42] Hongsheng Liu, Paolo Lazzaroni, and Cristiana Di Valentin. Nature of Excitons in Bidimensional WSe2 by Hybrid Density Functional Theory Calculations. *Nanomaterials*, 8(7):481, jun 2018.

[43] Claus F Klingshirn. *Chapter 9 Excitons, Biexcitons and Trions*. Graduate Texts in Physics. Springer Berlin Heidelberg, Berlin, Heidelberg, 2012.

[44] Masaki Shinada and Satoru Sugano. Interband optical transitions in extremely anisotropic semiconductors. I. Bound and unbound exciton absorption. *Journal of the Physical Society of Japan*, 21(10):1936–1946, dec 1966.

[45] Chitraleema Chakraborty, Kenneth M. Goodfellow, Sajal Dhara, Anthony Yoshimura, Vincent Meunier, and A. Nick Vamivakas. Quantum-Confined Stark Effect of Individual Defects in a van der Waals Heterostructure. *Nano Letters*, 17(4):2253–2258, apr 2017.

[46] Won Seok Yun, S. W. Han, Soon Cheol Hong, In Gee Kim, and J. D. Lee. Thickness and strain effects on electronic structures of transition metal dichalcogenides: 2H-MX 2 semiconductors (M = Mo, W; X = S, Se, Te). *Physical Review B - Condensed Matter and Materials Physics*, 85(3):033305, jan 2012.

[47] Chitraleema Chakraborty, Laura Kinnischtzke, Kenneth M. Goodfellow, Ryan Beams, and A. Nick Vamivakas. Voltage-controlled quantum light from an atomically thin semiconductor. *Nature Nanotechnology*, 10(6):507–511, jun 2015.

[48] Gui Bin Liu, Di Xiao, Yugui Yao, Xiaodong Xu, and Wang Yao. Electronic structures and theoretical modelling of two-dimensional group-VIB transition metal dichalcogenides, may 2015.

[49] Ashwin Ramasubramaniam. Large excitonic effects in monolayers of molybdenum and tungsten dichalcogenides. *Physical Review B - Condensed Matter and Materials Physics*, 86(11):115409, sep 2012.

[50] Andrea Splendiani, Liang Sun, Yuanbo Zhang, Tianshu Li, Jonghwan Kim, Chi Yung Chim, Giulia Galli, and Feng Wang. Emerging photoluminescence in monolayer MoS2. *Nano Letters*, 10(4):1271–1275, apr 2010.

[51] Achint Jain, Palash Bharadwaj, Sebastian Heeg, Markus Parzefall, Takashi Taniguchi, Kenji Watanabe, and Lukas Novotny. Minimizing residues and strain in 2D materials transferred from PDMS. *Nanotechnology*, 29(26):265203, may 2018.

[52] Hualing Zeng, Gui Bin Liu, Junfeng Dai, Yajun Yan, Bairen Zhu, Ruicong He, Lu Xie, Shijie Xu, Xianhui Chen, Wang Yao, and Xiaodong Cui. Optical signature of symmetry variations and spin-valley coupling in atomically thin tungsten dichalcogenides. *Scientific Reports*, 3(1):1–5, apr 2013.

[53] Xiao Xiao Zhang, Yumeng You, Shu Yang Frank Zhao, and Tony F. Heinz. Experimental Evidence for Dark Excitons in Monolayer WSe2. *Physical Review Letters*, 115(25):257403, dec 2015.

[54] Carmen Palacios-Berraquero. *Quantum Confined Excitons in 2-Dimensional Materials*. Springer, 2018.

[55] Sefaattin Tongay, Joonki Suh, Can Ataca, Wen Fan, Alexander Luce, Jeong Seuk Kang, Jonathan Liu, Changhyun Ko, Rajamani Raghunathanan, Jian Zhou, Frank Ogletree, Jingbo Li, Jeffrey C. Grossman, and Junqiao Wu. Defects activated photoluminescence in two-dimensional semiconductors: Interplay between bound, charged, and free excitons. *Scientific Reports*, 3(1):1–5, sep 2013.

[56] Hongyan Shi, Rusen Yan, Simone Bertolazzi, Jacopo Brivio, Bo Gao, Andras Kis, Debdeep Jena, Huili Grace Xing, and Libai Huang. Exciton dynamics in suspended monolayer and few-layer MoS2 2D crystals. *ACS Nano*, 7(2):1072–1080, feb 2013.

[57] Maurizia Palummo, Marco Bernardi, and Jeffrey C. Grossman. Exciton radiative lifetimes in two-dimensional transition metal dichalcogenides. *Nano Letters*, 15(5):2794–2800, may 2015.

[58] T. Korn, S. Heydrich, M. Hirmer, J. Schmutzler, and C. Schller. Low-temperature photocarrier dynamics in monolayer MoS2. *Applied Physics Letters*, 99(10), sep 2011.

[59] Yung Chang Lin, Torbjörn Björkman, Hannu Pekka Komsa, Po Yuan Teng, Chao Hui Yeh, Fei Sheng Huang, Kuan Hung Lin, Joanna Jadczak, Ying Sheng Huang, Po Wen Chiu, Arkady V. Krasheninnikov, and Kazu Suenaga. Threefold rotational defects in two-dimensional transition metal dichalcogenides. *Nature Communications*, 6(1):1–6, apr 2015.

[60] Shuai Zhang, Chen Guang Wang, Ming Yang Li, Di Huang, Lain Jong Li, Wei Ji, and Shiwei Wu. Defect Structure of Localized Excitons in a WSe2 Monolayer. *Physical Review Letters*, 119(4):046101, jul 2017.

[61] Lesheng Li and Emily A. Carter. Defect-mediated charge-carrier trapping and nonradiative recombination in WSe2 monolayers. *Journal of the American Chemical Society*, 141(26):10451–10461, 2019.

[62] Jianchen Dang, Sibai Sun, Xin Xie, Yang Yu, Kai Peng, Chenjiang Qian, Shiyao Wu, Feilong Song, Jingnan Yang, Shan Xiao, Longlong Yang, Yunuan Wang, M. A. Rafiq, Can Wang, and Xiulai Xu. Identifying defect-related quantum

emitters in monolayer WSe2. *npj 2D Materials and Applications*, 4(1):1–7, dec 2020.

[63] Jun Ichi Kasai and Yoshifumi Katayama. Low-temperature microphotoluminescence using confocal microscopy. *Review of Scientific Instruments*, 66(7):3738–3743, jul 1995.

[64] Attocube, https://www.attocube.com/application/files/7215/8443/7164/LT-APONIR0.81.pdf. *LT-APO/NIR/0.81*. (accessed: 2020-05-11).

[65] Wei Wu, Chandriker K. Dass, Joshua R. Hendrickson, Raul D. Montaño, Robert E. Fischer, Xiaotian Zhang, Tanushree H. Choudhury, Joan M. Redwing, Yongqiang Wang, and Michael T. Pettes. Locally defined quantum emission from epitaxial few-layer tungsten diselenide. *Applied Physics Letters*, 114(21):213102, may 2019.

[66] R Hanbury Brown and R.Q. Twiss. Interferometry of the intensity fluctuations in light - I. Basic theory: the correlation between photons in coherent beams of radiation. *Proceedings of the Royal Society of London. Series A. Mathematical and Physical Sciences*, 242(1230):300–324, nov 1957.

[67] MPD, http://www.micro-photon-devices.com/MPD/media/Datasheet/PDM.pdf. *PDM*, 4.5 edition, 11 2019. (accessed: 2020-05-11).

[68] Andres Castellanos-Gomez, Michele Buscema, Rianda Molenaar, Vibhor Singh, Laurens Janssen, Herre S J van der Zant, and Gary A Steele. Deterministic transfer of two-dimensional materials by all-dry viscoelastic stamping. *2D Materials*, 1(1):011002, apr 2014.

[69] Dan Bing, Yingying Wang, Jing Bai, Ruxia Du, Guoqing Wu, and Liyan Liu. Optical contrast for identifying the thickness of two-dimensional materials. *Optics Communications*, 406:128–138, jan 2018.

[70] Ashish Arora, MacIej Koperski, Karol Nogajewski, Jacques Marcus, Clément Faugeras, and Marek Potemski. Excitonic resonances in thin films of WSe2: From monolayer to bulk material. *Nanoscale*, 7(23):10421–10429, jun 2015.

[71] Jiani Huang, Thang B. Hoang, and Maiken H. Mikkelsen. Probing the origin of excitonic states in monolayer WSe2. *Scientific Reports*, 6(1):1–7, mar 2016.

[72] Dezheng Sun, Yi Rao, Georg A. Reider, Gugang Chen, Yumeng You, Louis Brézin, Avetik R. Harutyunyan, and Tony F. Heinz. Observation of rapid exciton-exciton annihilation in monolayer molybdenum disulfide. *Nano Letters*, 14(10):5625–5629, oct 2014.

[73] Bastian Miller, Alexander Steinhoff, Borja Pano, Julian Klein, Frank Jahnke, Alexander Holleitner, and Ursula Wurstbauer. Long-Lived Direct and Indirect Interlayer Excitons in van der Waals Heterostructures. *Nano Lett*, 17:5229–5237, 2017.

[74] Chandriker Kavir Dass, Mahtab A. Khan, Genevieve Clark, Jeffrey A. Simon, Ricky Gibson, Shin Mou, Xiaodong Xu, Michael N. Leuenberger, and Joshua R. Hendrickson. Ultra-Long Lifetimes of Single Quantum Emitters in Monolayer WSe ₂ /hBN Heterostructures. *Advanced Quantum Technologies*, 2(5-6):1900022, jun 2019.

[75] Aaron M. Jones, Hongyi Yu, Nirmal J. Ghimire, Sanfeng Wu, Grant Aivazian, Jason S. Ross, Bo Zhao, Jiaqiang Yan, David G. Mandrus, Di Xiao, Wang Yao, and Xiaodong Xu. Optical generation of excitonic valley coherence in monolayer WSe 2. *Nature Nanotechnology*, 8(9):634–638, aug 2013.